The Astrophysical Journal, 988:240 (18pp), 2025 August 1 https://doi.org/10.3847/1538-4357/ade2e4

Investigating the Physical Properties of Dusty Star-forming Galaxies at $z \gtrsim 1.5$ in the GOODS-South Field Using JWST

Dipanjan Mitra[1], Mattia Negrello[1], and Gianfranco De Zotti[2]
[1] School of Physics and Astronomy, Cardiff University, The Parade, CF24 3AA, UK; MitraD@cardiff.ac.uk, dipanmitra1@gmail.com
[2] INAF, Osservatorio Astronomico di Padova, Vicolo Osservatorio 5, I-35122, Padova, Italy
Received 2025 March 31; revised 2025 June 6; accepted 2025 June 7; published 2025 July 28

Abstract

We investigated how well the physical properties of progenitors of present-day massive spheroidal galaxies (protospheroids) can be constrained by the JWST Advanced Deep Extragalactic Survey (JADES) in the GOODS-South field, which benefits from extensive photometric and spectroscopic data, including those from the Hubble, Spitzer, and Herschel. We adopted a physical model for the evolution of protospheroidal galaxies, which form the bulk of dusty star-forming galaxies (DSFGs) at $z \gtrsim 1.5$ and confirmed its consistency with recent mid-infrared high-z galaxy luminosity functions. Using the model and the JADES survey strategy, we simulated a sample of protospheroids over 87.5 arcmin^2, matching the JADES/GOODS-S survey area. Photometric redshifts estimated from simulated JWST photometry showed $\gtrsim$95% accuracy and were used in spectral energy distribution fittings with Code Investigating GALaxy Emission (CIGALE). We demonstrated that JWST will provide reliable stellar mass estimates up to 0.1 dex for the majority of protospheroids at $z \gtrsim 1.5$ and can detect low-mass systems during cosmic noon that were inaccessible in the pre-JWST era. Focusing on the active star-forming phase of the protospheroid evolution, we defined a subsample flux limited at 250 μm (DSFG sample) and derived star formation rate, dust luminosity, and dust mass complementing the JWST photometry with that from Spitzer/MIPS and Herschel. We also constructed a JWST-selected DSFG catalog from ASTRODEEP data using NIRCam color criteria and demonstrated strong consistency between the observed and simulated DSFG populations.

Unified Astronomy Thesaurus concepts: High-redshift galaxies (734); Starburst galaxies (1570); Galaxy evolution (594); Galaxy photometry (611); Galaxies (573); Spectral energy distribution (2129); Stellar masses (1614)

1. Introduction

The discovery of dusty star-forming galaxies (DSFGs), also known as submillimeter galaxies (SMGs; I. Smail et al. 1997; A. J. Barger et al. 1998; D. H. Hughes et al. 1998), revolutionized our understanding of galaxy evolution, and the study of these high-z dusty sources became a crucial area of extragalactic astronomy. It is now widely agreed, based on several observational evidences, that high-z SMGs can be interpreted as being the progenitors of present-day massive spheroidal galaxies (S. J. Lilly et al. 1999; A. M. Swinbank et al. 2006; L. J. Hainline et al. 2011; J. M. Simpson et al. 2014, 2017; S. Toft et al. 2014; J. E. Birkin et al. 2024; C.-L. Liao et al. 2024; Q.-H. Tan et al. 2024; A. Amvrosiadis et al. 2025); in the following, these will be referred to as protospheroidal galaxies or protospheroids. This interpretation is consistent with the relatively old ages of stellar populations of nearby early-type galaxies (M. Bernardi et al. 2010; D. Thomas et al. 2010; S. Lu et al. 2023), implying that these galaxies formed the bulk of their stars at early times ($\log(\mathrm{age/yr}) \gtrsim 9.5$ corresponding to $z \gtrsim 1.5$), on a relatively short timescale, with high star formation rates (SFRs), and were quenched afterwards.

The fact that SMGs are frequently found to be gas-rich rotation-dominated disks (e.g., B. Gullberg et al. 2019; S. Gillman et al. 2023) is not in conflict with this interpretation. The extensive analysis of Atacama Large Millimeter/submillimeter Array (ALMA) submillimeter surface brightness profiles of SMGs by Q.-H. Tan et al. (2024) has highlighted that most of these galaxies are fully triaxial rather than flat disks. Other studies have pointed out that disky SMGs are dynamically hotter than local disk galaxies (i.e., have lower ratios of rotation to random velocity) and with a larger fraction of irregular morphologies (F. Lelli et al. 2016; A. M. Swinbank et al. 2017; O. J. Turner et al. 2017; E. Wisnioski et al. 2019; N. M. Förster Schreiber & S. Wuyts 2020; J. S. Kartaltepe et al. 2023; J. E. Birkin et al. 2024).

The pathway from SMGs to evolved spheroidal galaxies, implying kinematic and morphological evolution, is, however, still not completely clear. In our reference scenario (G. L. Granato et al. 2004; Z.-Y. Cai et al. 2013; A. Lapi et al. 2014), high-z SMGs evolve to the galaxy main sequence, with lower dust-to-stellar-mass ratios and substantially lower specific SFR compared to SMGs (C. Mancuso et al. 2016), and end in passive evolution. In this process, their stellar mass grows while their dust obscuration decreases as a result of supernova and active galactic nucleus (AGN) feedback, which sweep off the interstellar medium.

So far, the observational assessment of the evolutionary history of spheroidal galaxies has been hampered by the limited depth and poor angular resolution of the instruments. The next generation instruments already launched like the James Webb Space Telescope (JWST; J. P. Gardner et al. 2006; J. Rigby et al. 2023; M. W. McElwain et al. 2023), the Euclid space observatory (R. Laureijs et al. 2011), and those in preparation like the Vera C. Rubin Legacy Survey of Space and Time (Ž. Ivezic et al. 2019) will be able to overcome the

above limitations with unprecedented sensitivity and resolution.

In this paper, we investigate the potential of the JWST Advanced Deep Extragalactic Survey (JADES; D. J. Eisenstein et al. 2023) for shedding light on the protospheroid evolution. We adopt the standard approach, exploiting models to simulate the survey outcome. A phenomenological model specifically designed to simulate JWST extragalactic surveys was presented by C. C. Williams et al. (2018) who applied it to make predictions for the JADES in GOODS-South and GOODS-North fields (M. Giavalisco et al. 2004), aiding their optimization and the interpretation of the data. These fields are among the best-studied extragalactic deep fields with the availability of a large amount of photometric and spectroscopic data from the ultraviolet to the far-IR (FIR), including data from the Hubble Space Telescope (HST), Spitzer, and Herschel (D. Liu et al. 2018; G. Barro et al. 2019).

In this paper, we exploit the model by Z.-Y. Cai et al. (2013), which coevolves massive protospheroids and the central AGN at $z \gtrsim 1.5$. It is a physical model, therefore well suited to link the observational data to the physics driving the early galaxy evolution. Importantly, the model captures the full life cycle of massive galaxies: starting with an initial UV-bright star-forming phase, followed by a heavily dust-enshrouded starburst phase (corresponding to the DSFG stage), then transitioning through a short-lived quasar phase, before settling into passive evolution.

We adopt the version upgraded by D. Mitra et al. (2024), which links the model outputs to the formalism by E. da Cunha et al. (2008) and by J. Fritz et al. (2006) to compute the spectral energy distributions (SEDs) of DSFG and of AGN components, respectively. The model was used by D. Mitra et al. (2024) to study the ability of Euclid in constraining the physical properties of DSFGs at $z \gtrsim 1.5$ detected by the Herschel Astrophysical Terahertz Large Area Survey (S. Eales et al. 2010).

In the pre-JWST era, several studies have been conducted to estimate the physical properties of DSFGs in the GOODS-S field. M. Franco et al. (2020) studied a sample of 35 galaxies detected with ALMA at 1.1 mm in the GOODS-ALMA field (M. Franco et al. 2018). To derive their physical properties, they performed SED fitting using the available multiwavelength data. The sample comprised massive galaxies having a median stellar mass estimate of $8.5 \times 10^{10} M_{\odot}$ in the redshift range $z \sim$ 2–4. Y. Yamaguchi et al. (2020) estimated the physical properties of a sample of 24 *K*-band selected galaxies from the Four Star Galaxy Evolution Survey (ZFOURGE; C. M. S. Straatman et al. 2016) having deep 1.2 mm ALMA observations, as a part of the ALMA twenty-six Arc minute[2] Survey of GOODS-S at One-millimeter.[3] With a median redshift of 2.38 ± 0.14, these sources have median stellar mass estimates of $\log(M_{\star}/M_{\odot}) \sim 10.75$ in both redshift bins $1 < z \leqslant 2$ and $2 < z \leqslant 3$. In the same redshift bins, the obtained medians $\log(\dot{M}_{\star}/M_{\odot}\ \mathrm{yr}^{-1})$ were 2.14 and 2.15, respectively. T. Wiklind et al. (2014) studied a sample of 10 submillimeter sources observed with ALMA at 870 μm originally detected using LABOCA (G. Siringo et al. 2009) in the Cosmic Assembly Near-infrared Deep Extragalactic Legacy Survey (CANDELS) of the GOODS-S. A median stellar mass estimate of $9.1 \times 10^{10} M_{\odot}$ was obtained. The average SFR obtained was $(0.8 \pm 0.7) \times 10^3\, M_{\odot}\ \mathrm{yr}^{-1}$. A panchromatic study of 11 DSFGs with spectroscopic redshift $1.5 < z_{\mathrm{spec}} < 3$ in the GOODS-S field was conducted by L. Pantoni et al. (2021). They performed SED fitting using CIGALE and estimated the median stellar mass and SFR of the sources to be $6.5 \times 10^{10} M_{\odot}$ and $241\ M_{\odot}\ \mathrm{yr}^{-1}$, respectively. As can be seen, the studies conducted so far on DSFGs in the GOODS-S could only probe median stellar masses down to about $\log(M_{\star}/M_{\odot}) \approx 10.8$. In this work, we also try to investigate the minimum stellar mass at which JWST can reliably detect DSFGs.

The paper is organized as follows. Section 2 gives a brief description of the model. In Section 3, we provide a concise presentation of the relevant surveys. Section 4 presents a comparison of physical properties of ASTRODEEP-JWST sources with model predictions. Finally, Section 5 contains the summary and the conclusions of this paper. Here, we adopt a flat ΛCDM cosmology with present-day matter density (in units of the critical density), $\Omega_{m,0} = 0.3153$, and baryon density $\Omega_{b,0} = 0.0493$. We set the value of the Hubble–Lemaître constant to $h = H_0/100 = 0.6736$, the slope of the spectrum of primordial density perturbations to $n = 0.9649$, and the normalization of the density fluctuations on a scale of $8h^{-1}$ Mpc to $\sigma_8 = 0.8111$ (Planck Collaboration VI 2020).

2. Methodology

2.1. Model Outline

The Z.-Y. Cai et al. (2013) model was inspired by the fact that the stellar content of present-day massive spheroidal galaxies is dominated by old populations, formed at $z \gtrsim 1.5$. In contrast, the disk-shaped galaxies contain relatively young stellar populations, with a luminosity-weighted age $\lesssim$7 Gyr, i.e., mostly formed at $z \lesssim 1$. Therefore, at $z \gtrsim 1.5$, the dominant star-forming galaxies are the protospheroidal galaxies, the progenitors of the present-day ellipticals. This physical treatment takes into account the coevolution of the SFR of the protospheroids and of the supermassive black holes (SMBHs) residing at their center.

The star formation history (SFH) of these protospheroids is determined by a set of equations that describe the gas cooling and condensation into stars, the accretion of the gas into the SMBH, as well as the feedback from the supernova explosions and from the AGN. We refer the readers to Z.-Y. Cai et al. (2013) and D. Mitra et al. (2024) for more detailed explanations about the equations governing the coevolution of the stellar components and of the AGN components.

The SED of the photo-spheroids is modeled using the formalism put forward by E. da Cunha et al. (2008), which is based on the principle of energy balance, with a few modifications explained in detail in D. Mitra et al. (2024). We adopt the smooth torus model introduced by J. Fritz et al. (2006) to model the SED of the AGN component. In modeling the dust emission from the AGN, we do not incorporate the contribution from polar dust (S. F. Hnig et al. 2013; Q. Yang et al. 2020) as it emits mostly in the mid-IR (MIR) and has a negligible effect at UV/optical/near-IR (NIR) wavelengths (S. F. Hnig et al. 2013, see their Figure 8).

To verify that this modified version of Cai's model correctly predicts the luminosity functions (LFs) of protospheroidal

[3] https://sites.google.com/view/asagao26/home

galaxies at MIR wavelengths, we computed the rest-frame LFs of these galaxies at 7.7, 10, 12.8, 15, 18, and 21 μm, respectively, and compared them with the rest-frame LFs produced by C.-T. Ling et al. (2024) using a sample of 506 galaxies at $z = 0$–5.1 from the JWST Cosmic Evolution Early Release Science (CEERS; S. L. Finkelstein et al. 2017) survey. Figure 1 shows the plot of the MIR LFs for redshift $z = 1.8$, 2.5, and 3.5, respectively.

It is to be noted that the values of model parameters are not optimized, i.e., no fit of the data was attempted. The model curve (red) shows the contribution of galaxies with virialized halo masses in the range $11.3 \leqslant \log(M_{\rm vir}/M_{\odot}) \leqslant 13.3$ (see D. Mitra et al. 2024; and sub-Section 2.3). The adopted lower limit to halo masses translates to a fast decrease of the model LFs at low luminosities, where less massive galaxies dominate. As a consequence, the model underpredicts the low-luminosity end of LFs. Decreasing the minimum halo mass would make the model predictions less solid. This is because a basic assumption of the model, namely, that the halo formation rate is well approximated by the positive term of the cosmic time derivative of the halo mass function, is less accurate at low halo masses.

At high luminosity, the consistency with observations is satisfactory, especially considering that the model is not optimized. At some combinations of rest-frame wavelength and redshift, the complexity of the SED at MIR wavelengths, where the polycyclic aromatic hydrocarbon (PAH) features are prominent, can also contribute to the small discrepancy between the predicted and the measured LFs. In fact, such a complexity is not fully captured by our formalism, which adopts only a single template for the PAHs.

2.2. NIRCam Color Comparison between CEERS and the Model

To further evaluate the realism of our simulated protospheroidal galaxies, we compare their NIR colors to galaxies observed in the CEERS survey using a F150W − F277W versus F277W − F444W color–color diagram as shown in Figure 2. The CEERS sources, shown in gray, are taken from the ASTRODEEP-JWST catalog (E. Merlin et al. 2024; for more details, see Section 4.3) and span a broad range of redshifts, dust contents, and stellar populations, forming a wide distribution in the color–color plane. In contrast, the simulated protospheroids (cyan points) occupy a more confined region. Notably, these galaxies follow a trend consistent with high-redshift star-forming systems, with moderate to substantial dust obscuration. Overlaid on the plot are evolutionary tracks of dusty galaxies based on V-band dust attenuation (A_V) and redshifted from $z = 1$ to 6 by A. S. Long et al. (2024). These tracks illustrate how dust attenuation and redshift drive the observed colors. The lower, middle, and upper tracks correspond to $A_V < 1$ (little attenuation), $A_V \sim 2$ (average attenuation), and $A_V \gtrsim 3$ (high attenuation), respectively. They obtain these evolutionary tracks using the SEDs of ALESS SMGs from E. da Cunha et al. (2015). The majority of the simulated DSFGs cluster at a moderate attenuation, consistent with the expected properties of protospheroids at $z \gtrsim 1.5$.

2.3. Building the Simulated Catalog

Here, we give a brief explanation about the generation of a simulated sample of protospheroidal galaxies to be used for the forecast and analysis. The building of the simulated catalog starts by randomly sampling the formation rate function of dark matter haloes (see Equation (A25) of D. Mitra et al. 2024) in both the virialization mass ($M_{\rm vir}$) and the virialization redshift ($z_{\rm vir}$) of the halos. We restrict ourselves to the ranges $11.3 \leqslant \log(M_{\rm vir}/M_{\odot}) \leqslant 13.3$ and $1.5 \leqslant z_{\rm vir} \leqslant 8$, respectively.

The number of sampled halos depends on the size of the surveyed area of the sky. Here, we consider a survey area of 87 arcmin^2, like that covered by the JADES-Medium survey in the GOODS-S field. We then allow the baryons within the simulated halos to evolve into galaxies by solving the equations of the model by Z.-Y. Cai et al. (2013) to get the SFH and the black hole accretion rate as a function of the galaxy age. The galaxy is assumed to be born at $z_{\rm vir}$. Next, we generate the SEDs of both the stellar components and the AGN components of simulated galaxies. We refer the readers to D. Mitra et al. (2024) for a detailed description of the steps involved and of the adopted values of the different parameters.

3. Forecasts

Here, we investigate to what extent JWST can constrain the physical properties of high-z protospheroids along with the minimum stellar mass at which JWST can reliably detect them in the GOOD-S field, the primary JADES field. Since the CANDELS studied the GOODS-S field using HST, we also complement the JWST data with the HST data. IR and submillimeter data from Spitzer and Herschel are also available for this field. We examine the effect on the physical parameters by considering different combinations of data from UV to IR/submillimeter with JWST photometry from JADES. To begin with, we provide a brief summary of the CANDELS and of the JADES survey programs and then proceed with the results and the analysis.

3.1. A Brief Overview of the CANDELS and JADES Survey

The CANDELS (N. A. Grogin et al. 2011; A. M. Koekemoer et al. 2011) was designed to study galaxy formation and evolution over the $1.5 \leqslant z \leqslant 8$ range. The main idea behind it was to exploit the revolutionary NIR HST/WFC3 camera for obtaining deep imaging of distinct faint objects. Parallel observations using HST/Advanced Camera for Surveys (ACS) were also carried out, to provide multiwavelength coverage of galaxies. The survey covered 800 arcmin^2 of the sky in five fields: GOODS (both North and South; M. Giavalisco et al. 2004), Ultra Deep Survey (UDS; A. Lawrence et al. 2007), Extended Groth Strip (EGS; M. Davis et al. 2007), and Cosmic Evolution Survey (COSMOS; N. Scoville et al. 2007). The HST filters used in CANDELS are F435W, F606W, F775W, F814W, and F850LP for HST/ACS; and F098M, F105W, F125W, and F160W filters for HST/WFC3. Table 1 gives the 5σ point-source sensitivity values of the HST filters used, from Y. Guo et al. (2013). The CANDELS/GOODS survey also has MIR/FIR observations from Spitzer (MIPS, 24, 70 μm) and Herschel (PACS, 100, 160 μm; SPIRE, 250, 350, and 500 μm). The table also provides the 5σ limits for the FIR filters, from G. Barro et al. (2019).

The JADES (D. J. Eisenstein et al. 2023) is a joint project of the NIRCam (M. J. Rieke et al. 2023) and NIRSpec (P. Jakobsen et al. 2022) Instrument Development teams. JADES is the

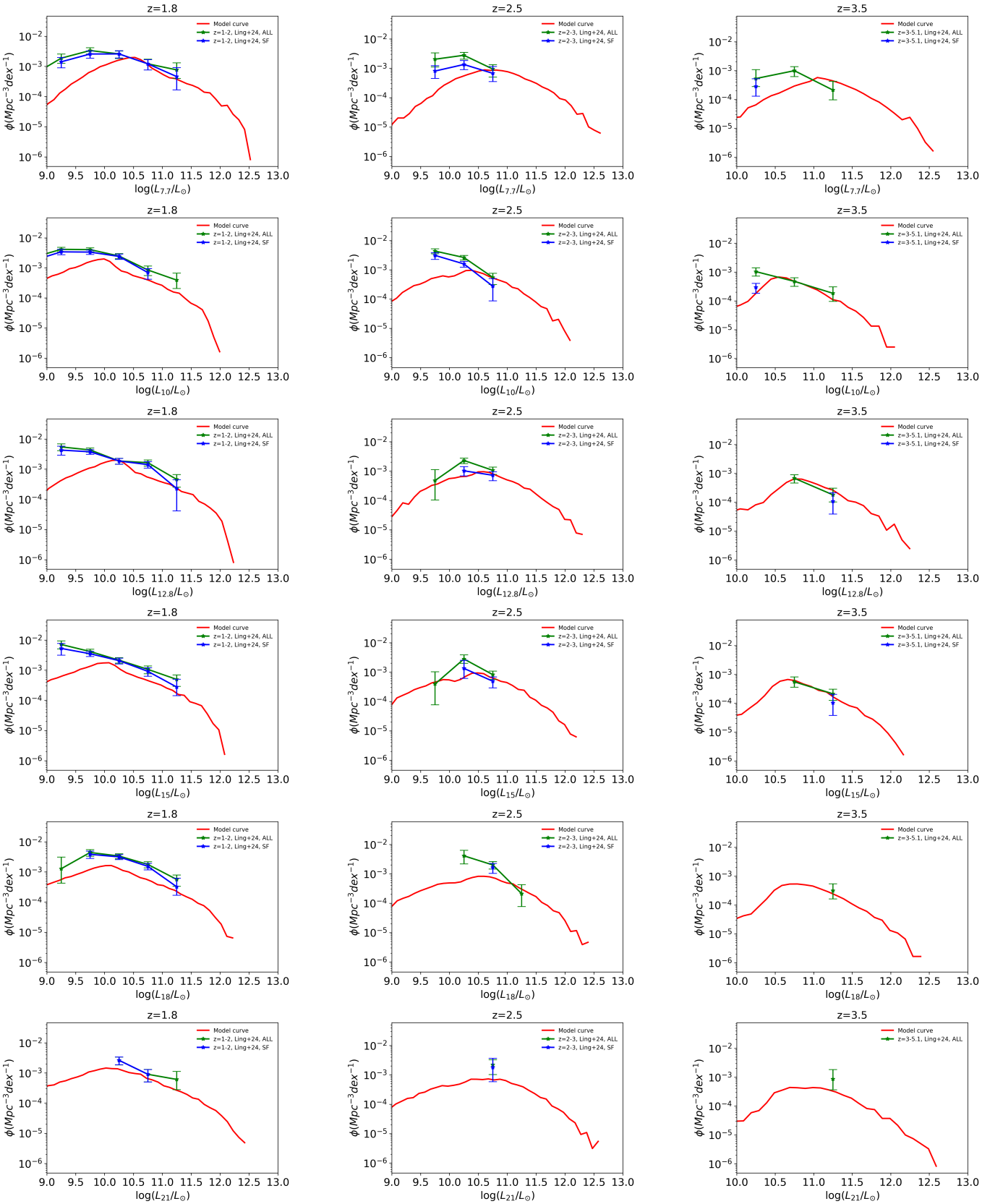

Figure 1. Comparison of the measured monochromatic LFs with those predicted for the population of massive ($11.3 \leqslant \log(M_{\rm vir}/M_\odot) \leqslant 13.3$) protospheroids at 7.7, 10, 12.8, 15, 18, and 21 μm for $z = 1.8$, 2.5, and 3.5. The red line shows the model curve. Note that the model parameters were not optimized; no fit of the data was attempted. At low luminosity, the dominant contribution to the LFs comes from galaxies with halo masses below the adopted lower limit. This leads to a fast decrease of the model curve at low luminosity, implying an underprediction of the LFs. The green line shows the LF from C.-T. Ling et al. (2024) for all galaxy populations, while the blue line shows the same for the star-forming (SF) galaxies. The first column shows the data points for the redshift bin $z = 1$–2, the middle column for $z = 2$–3, and the last column for $z = 3$–5.1.

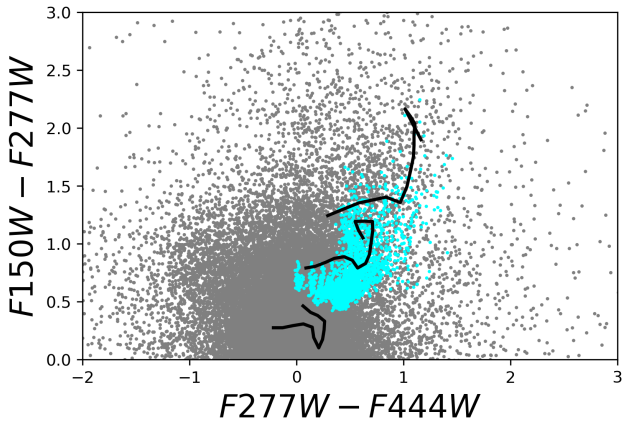

Figure 2. JWST/NIRCam F150W − F277W vs. F277W − F444W color–color diagram. Gray points represent observed galaxies from the CEERS survey (taken from the ASTRODEEP-JWST catalog), and cyan points show simulated protospheroids from our model. The black curves represent evolutionary tracks from redshift $z \sim 1$ to 6 for galaxies with different dust attenuations: $A_V < 1$ (bottom), $A_V \sim 2$ (middle), and $A_V \gtrsim 3$ (top). The model galaxies align well with the moderately to heavily obscured tracks, indicating a good consistency between simulated and observed color distributions.

Table 1
HST, JWST, Spitzer, and Herschel Filters Along with Their Central Wavelengths and 5σ Depths (5σ Depths Are in AB Magnitudes Except for Spitzer and Herschel)

Filter	Central Wavelength (μm)	5σ Depth
F435W/ACS/HST	0.436	28.95
F606W/ACS/HST	0.603	29.35
F775W/ACS/HST	0.773	28.55
F814W/ACS/HST	0.813	28.84
F850LP/ACS/HST	0.908	28.55
F098M/WFC3/HST	0.990	28.77
F105W/WFC3/HST	1.065	28.45
F125W/WFC3/HST	1.257	28.34
F160W/WFC3/HST	1.543	28.16
F090W/NIRCam/JWST	0.98	28.85
F115W/NIRCam/JWST	1.162	28.98
F150W/NIRCam/JWST	1.510	28.93
F200W/NIRCam/JWST	2.002	29.02
F277W/NIRCam/JWST	2.784	29.32
F335M/NIRCam/JWST	3.367	28.89
F356W/NIRCam/JWST	3.593	29.32
F410M/NIRCam/JWST	4.088	28.87
F444W/NIRCam/JWST	4.439	29.03
Spitzer/MIPS	24	0.03 mJy
Spitzer/MIPS	70	2.5 mJy
Herschel/PACS	100	1.1 mJy
Herschel/PACS	160	3.4 mJy
Herschel/SPIRE	250	8.3 mJy
Herschel/SPIRE	350	11.5 mJy
Herschel/SPIRE	500	11.3 mJy

Note. The JWST limiting magnitudes refer to JADES-Medium.

largest program being conducted in the Cycle 1 run of JWST with an observing time of 770 hr; it observes two of the best-studied deep fields, namely, GOODS-South and GOODS-North. The main focus is on GOODS-S, which includes the Chandra Deep Field South (R. Giacconi et al. 2002) and the Hubble Ultra Deep field (S. V. W. Beckwith et al. 2006). Along with that, deep ALMA (M. Franco et al. 2018; B. Hatsukade et al. 2018) and JVLA data (S. Alberts et al. 2020) are available for this field. The GOODS-N, which contains the Hubble deep field and was covered by a deep Chandra survey, was chosen as the second field.

The design of JADES is like a two-layer wedding cake comprising deep portions of both imaging and spectroscopic data, along with medium-depth surveys over larger areas. The continuous portions of NIRCam imaging are named as "prime" while those with parallel NIRSpec exposures are designated as "parallel." JADES-Deep comprises a survey area of 36 arcmin^2 while JADES-Medium covers 175 arcmin^2. The JADES-Deep survey will be carried out only on GOODS-S. The survey area of JADES-Medium is almost equally distributed between the GOODS-N and the GOODS-S fields. NIRCam imaging in JADES is done using nine filters, namely, F090W, F115W, F150W, F200W, F277W, F335M, F356W, F410M, and F444W. The mean wavelength and the 5σ depth for each filter are given in Table 1.

3.2. Simulation Setup

A source in the simulated catalog is said to be detected by JWST if its flux density is >5σ in all the NIRCam bands. To incorporate HST photometry, we apply the 5σ detection criteria to ACS/F435W and WFC3/F160W filters on JWST-detected sources. For Herschel, we adopt the 5σ detection limit in the SPIRE 250 μm band. Among these sources, we say a source is detected by Spitzer/MIPS if it has a flux density >5σ at both 24 and 70 μm.

To investigate the detectability of protospheroids by JWST, we have simulated galaxies having a virialized halo mass in the range $11.3 \leqslant \log(M_{\rm vir}/M_{\odot}) \leqslant 13.3$. We call this the "parent sample"; it comprises 27,748 galaxies detected at 5σ in all nine NIRCam bands. Approximately 41% of them are also detected by HST above 5σ in the F435W and F160W bands. However, only 1.5% and 1.7% of these JWST sources are detected above 5σ by Spitzer and Herschel, respectively. While JWST can help to constrain the stellar mass of galaxies, FIR observations are crucial in constraining the SFR of DSFGs.

To get a larger fraction of detections by Herschel and Spitzer, we simulated all galaxies with $12 \leqslant \log(M_{\rm vir}/M_{\odot}) \leqslant 13.3$; galaxies with $\log(M_{\rm vir}/M_{\odot}) < 12$ are undetected by Herschel. In this subsample, there are 507 galaxies above the Herschel 5σ detection limit at 250 μm; these constitute our DSFG sample. Among them, 503 galaxies, approximately 99%, are detected at 5σ in all nine NIRCam bands. HST detects ≈98.8% of these DSFGs, while 434 (≈86%) are detected in both Spitzer/MIPS bands at >5σ.

3.3. Estimation of Photometric Redshifts and Galaxy Physical Properties

To estimate the physical properties of galaxies, the knowledge of redshifts is essential. Therefore, the first thing that we estimated for our simulated sample was the redshift from the JWST photometry. Since the HST photometry is available for most of the sources, we also estimated the photometric redshift by complementing the JWST photometry with that from HST.

We used the template-based photo-z estimation code Easy and Accurate Redshifts from Yale (EAZY; G. B. Brammer et al. 2008). This code is applicable for the estimation of photo-z using UV/optical/NIR photometric data. We use "v1.3" of EAZY, which uses nine templates. The original five templates of "v1.0" of EAZY are from A. Grazian et al. (2006). The dusty galaxies are taken into account by adding a starburst template with $t = 50$ Myr and $A_V = 2.75$. The evolved simple stellar population (SSP) model by C. Maraston (2005) is added to include massive old galaxies at $z < 1$. The dust template is taken from D. K. Erb et al. (2010). The P. Madau (1995) model for dust absorption by the intergalactic medium is also taken into account in EAZY. A redshift range of $z = 1$–8 in steps of $\Delta z = 0.01$ was chosen.

After estimating the photo-z, we proceeded to estimate the physical properties of the simulated galaxies. For this, we used the SED fitting code CIGALE (D. Burgarella et al. 2005; S. Noll et al. 2009; M. Boquien et al. 2019), which uses the principle of "energy balance," i.e., the amount of stellar energy absorbed by dust in the UV/optical regime is entirely processed and reemitted at FIR/submillimeter wavelengths, to build the panchromatic model of the SEDs of galaxies. The SED templates generated by CIGALE depend on the modules and values of different parameters chosen by the user. In this work, we adopted a delayed SFH with an additional late burst of star formation. The G. Bruzual & S. Charlot (2003) SSP models along with a Chabrier initial mass function (G. Chabrier 2003) and solar metallicity are chosen. The S. Charlot & S. M. Fall (2000) model is used for modeling the dust attenuation. The dust emission is modeled following B. T. Draine et al. (2014). To incorporate the contribution from the AGN, templates from J. Fritz et al. (2006) are used. With the above-chosen modules and parameter values (see Table 2), CIGALE generated around 6 billion SED templates and then used a χ^2 minimization technique to get the best-fit SED and estimate the physical properties (S. Noll et al. 2009).

Table 2
Parameter Values Given as Input to CIGALE for SED Fitting

SFH: sfhdelayed—Delayed SFH with Optional Exponential Burst	
e-folding time of the main stellar population (Myr)	500, 1000, 2000, 3000, 4000, 5000, 6000, 7000
e-folding time of the late starburst population (Myr)	1000, 5000, 10000
mass fraction of the late starburst population	0.0, 0.001, 0.01, 0.1, 0.15, 0.3, 0.5
age of the main stellar population (Myr)	500, 1000, 2000, 3000, 5000, 6000, 7000, 8000, 9000, 10000
age of the late starburst (Myr)	10, 30, 50, 70, 100, 150, 300
SSP: bc03	
initial mass function (IMF)	Chabrier
metallicity	0.02 ($Z_\odot$), 0.008
Dust Attenuation: dustatt_modified_CF00	
V-band attenuation in ISM ($A_V^{\rm ISM}$)	0.3, 0.5, 0.9, 1.1, 1.7, 2.0
μ	0.44
power-law slope of attenuation in the ISM	−0.7, −1.3
power-law slope of attenuation in the stellar BCs	−0.7, −1.3
Dust Emission: dl2014	
PAH mass fraction ($q_{\rm PAH}$, in %)	2.5, 3.9, 4.58, 7.32
minimum radiation field ($U_{\rm min}$) (Habing)	20, 25, 50
dust emission power-law slope (α)	2, 3
fraction illuminated from $U_{\rm min}$ to $U_{\rm max}$ (γ)	0.02
AGN: fritz2006	
ratio of the maximum to minimum radii of the dusty torus ($r_{\rm ratio}$)	60, 100, 150
equatorial optical depth at 9.7 μm (τ)	0.6, 10.0
radial dust distribution within the torus (β)	0.0
angular dust distribution within the torus (γ)	6
full opening angle of the dusty torus (opening angle)	100
angle between the equatorial axis and line of sight (Ψ)	0.001, 89.990
AGN fraction ($f_{\rm AGN}$)	0.0, 0.1, 0.15, 0.25, 0.5

Note. The modules chosen for the various components of CIGALE are shown in bold.
ISM (interstellar medium).
References. S. Charlot & S. M. Fall 2000, G. Bruzual & S. Charlot 2003, G. Chabrier 2003, J. Fritz et al. 2006, B. T. Draine et al. 2014.

4. Results

In this section, we discuss the results obtained for the photometric redshifts and for the physical properties of the JWST-detected simulated galaxies.

4.1. Derived Photometric Redshift

The scatter plot of the photometric redshifts estimated from the JWST photometry alone versus the input redshifts is shown in the left-hand panel of Figure 3 for both the parent catalog (top panel) and the DSFG subsample (bottom panel) of galaxies. We observe that JWST provides a good redshift estimate up to $z \sim 4$ for both the parent sample and the subsample. The outlier fraction, defined as $|\Delta z|/(1 + z_{\rm input}) > 0.15$ where $|\Delta z| = |z_{\rm input} - z_{\rm phot}^{\rm EAZY}|$ (C. Laigle et al. 2016), is $f_{\rm outlier} = 0.05$ for the parent sample and $f_{\rm outlier} = 0.042$ for the DSFG subsample, respectively. The most catastrophic errors on z occur in the range $4 \leqslant z \leqslant 5$–$6$, where there is a leakage of high-z sources to the low-redshift regime. Also, a few galaxies at $z \sim 2$ are wrongly assigned a redshift $z > 4$. These wrong estimations of redshift are mostly due to the degeneracy between the Lyman-α break at 912 and the 4000 break. The right-hand panels of Figure 3 show the estimated versus true photo-z values for the JWST sources, which are also detected by HST. We observe that, on complementing the JWST photometry with that from HST, most of the low-z contaminants are removed, and we get a very good level of agreement between the input and the estimated photo-z values at all redshifts up to $z \leqslant 5$. Thanks to the availability of the HST photometry, EAZY can properly sample the Lyman break, and the degeneracy with the 4000 break is rectified. This is because, at $z \sim 4$–5, the Lyman break is missed by the JWST NIRCam filters, but it falls within the HST filters. However, for the parent sample, there are still some catastrophic redshift determinations. These are mostly

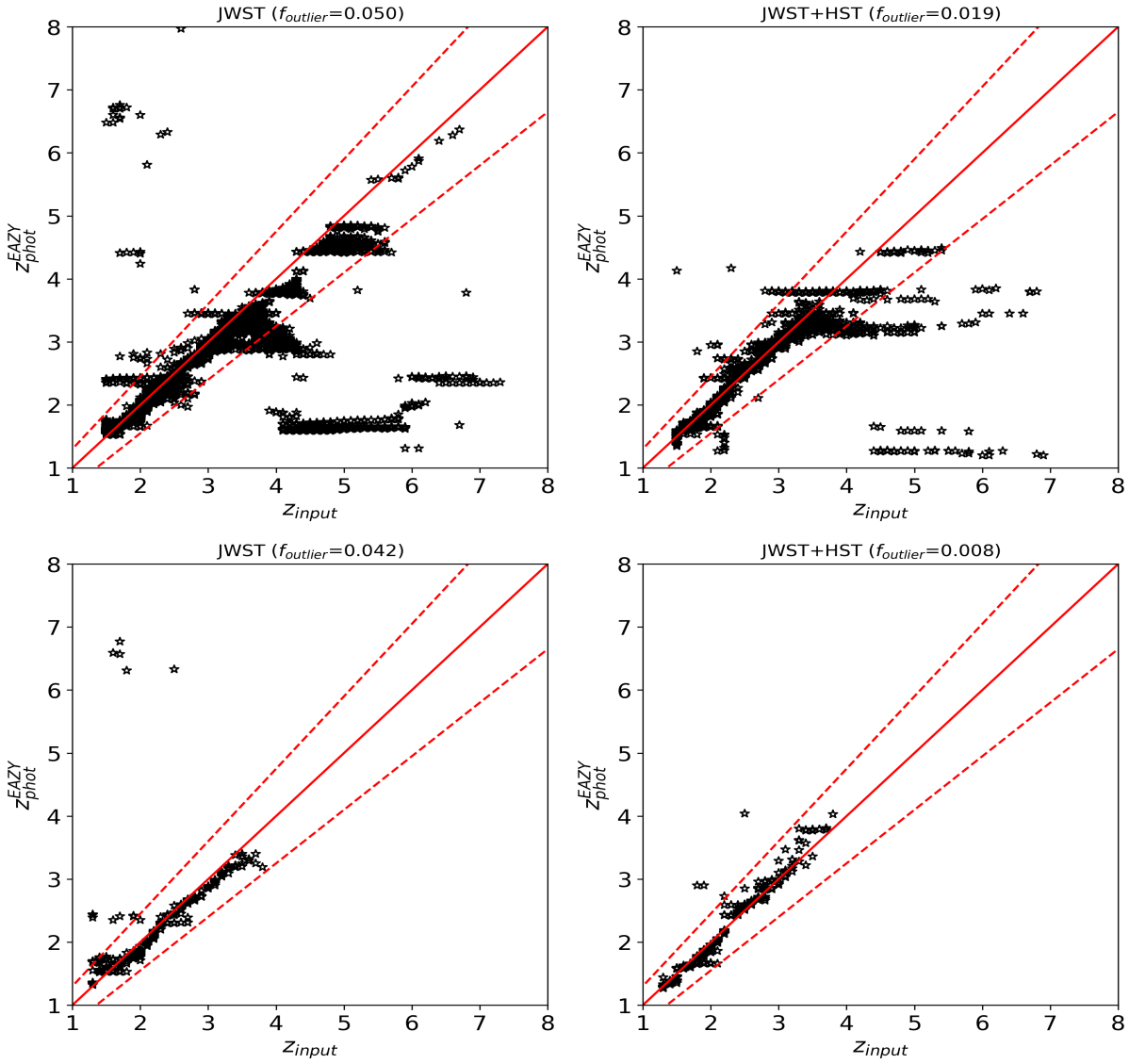

Figure 3. Derived photometric redshift using EAZY vs. input redshift of the galaxies detected by JWST at $>5\sigma$ in all nine NIRCam bands, also detected by the HST at $\geqslant 5\sigma$ in the F435W and F160W bands. The solid red line denotes $z_{\rm input} = z_{\rm phot}^{\rm EAZY}$ while the dashed red lines define the region where $|\Delta z| \leqslant 0.15(1 + z_{\rm input})$. Top row refers to the parent sample while the bottom row is for DSFG subsample (detected at $\geqslant 5\sigma$ at 250 μm, i.e., having $S_{250\mu{\rm m}} \geqslant 8.3$ mJy). Most catastrophic outliers (black patches toward the bottom right of the top panel), i.e., sources having $z_{\rm input} \gtrsim 4$ and low $z_{\rm phot}^{\rm EAZY}$, are AGN dominated. In other cases, catastrophic errors are due to the degeneracy between the Lyα break at 912 and the 4000 break.

AGN-dominated sources, the SEDs of which are featureless and power law shaped, which makes it difficult for EAZY to give a correct estimation of redshift. The outlier fraction, for the JWST+HST photometry, is reduced to $f_{\rm outlier} = 0.019$ and $f_{\rm outlier} = 0.008$ for the parent sample and the DSFG subsample, respectively. Overall, the recovery of redshifts for DSFGs using JWST photometry demonstrates excellent performance, with high accuracy and remarkably low outlier fractions. The broad wavelength coverage and the high sensitivity of NIRCam enable reliable photometric redshift estimates even for heavily dust-obscured systems. This highlights JWST's unique capability to precisely constrain the redshift distribution of DSFGs, which has been a major challenge for previous infrared and optical surveys.

For the DSFG sample, we attempted to estimate photometric redshifts using Herschel/SPIRE photometry based on the E. A. Pearson et al. (2013) template set. However, this approach resulted in a high outlier fraction of approximately 33%. Even after restricting the analysis to sources with additional 5σ detections at both 350 and 500 μm, the outlier fraction remained high, at 28%. Due to this significant level of inaccuracy, we do not adopt the FIR-based redshift estimates in our analysis. Instead, we rely on photometric redshifts estimated using EAZY applied to JWST photometry for the rest of our analysis.

4.2. Derived Physical Properties

The estimation of physical properties like stellar mass ($M_\star$), SFR ($\dot{M}_\star$), dust luminosity ($L_{\rm dust}$), and dust mass ($M_{\rm dust}$), of the JWST-detected simulated galaxies is done using CIGALE by setting the redshift to the value derived by EAZY. Also, we discuss the improvement that JWST NIRCam photometry

Table 3
Median Values Along with the Median Absolute Deviation of the Estimated Physical Quantities for the Parent Sample (Where the Simulated Galaxies Have Virialized Halo Mass in the Range $11.3 \leqslant \log(M_{\rm vir}/M_{\odot}) \leqslant 13.3$) and the DSFG Subsample (Having Flux Density $\gtrsim$8.3 mJy at 250 μm), Respectively

	$\log(M_{\star}/M_{\odot})$	$\log(\dot{M}_{\star}/M_{\odot}\ {\rm yr}^{-1})$	$\log(L_{\rm dust}/L_{\odot})$	$\log(M_{\rm dust}/M_{\odot})$
Parent Sample				
JWST	9.81 ± 0.16	⋯	⋯	⋯
JWST+HST	9.89 ± 0.23	⋯	⋯	⋯
Subsample				
JWST	10.8 ± 0.23	⋯	⋯	⋯
JWST+HST	10.86 ± 0.23	⋯	⋯	⋯
Spitzer+Herschel	⋯	2.21 ± 0.3	12.34 ± 0.26	8.5 ± 0.26
HST+Spitzer+Herschel	10.8 ± 0.3	2.5 ± 0.21	12.5 ± 0.23	8.5 ± 0.23
JWST+Spitzer+Herschel	10.83 ± 0.27	2.52 ± 0.22	12.48 ± 0.22	8.6 ± 0.22
JWST+HST+Spitzer+Herschel	10.83 ± 0.27	2.52 ± 0.23	12.5 ± 0.23	8.6 ± 0.23

Table 4
Mean (Median) Values of $Q_{\log P}$ for the Parent Sample (Where the Simulated Galaxies Have Virialized Halo Mass in the Range $11.3 \leqslant \log(M_{\rm vir}/M_{\odot}) \leqslant 13.3$) and the DSFG Subsample (Having 5σ Flux Density $\gtrsim$8.3 mJy at 250 μm), Respectively

	$Q_{\log(M_{\star})}$	$Q_{\log(\dot{M}_{\star})}$	$Q_{\log(L_{\rm dust})}$	$Q_{\log(M_{\rm dust})}$
Parent Sample				
JWST	−0.14(−0.132)	⋯	⋯	⋯
JWST+HST	−0.068(−0.083)	⋯	⋯	⋯
Subsample				
JWST	−0.004(−0.017)	⋯	⋯	⋯
JWST+HST	0.035(0.055)	⋯	⋯	⋯
Spitzer+Herschel	⋯	−0.196(−0.24)	0.075(0.085)	−0.012(−0.033)
HST+Spitzer+Herschel	0.01(−0.02)	0.037(0.056)	−0.006(−0.077)	0.124(0.12)
JWST+Spitzer+Herschel	−0.0169(−0.039)	0.044(0.032)	−0.049(−0.045)	0.15(0.13)
JWST+HST+Spitzer+Herschel	−0.04(−0.052)	0.053(0.066)	−0.066(−0.077)	0.13(0.13)

Note. The corresponding plots are shown in Sections 4.2.1., 4.2.2., and 4.2.3., respectively.

brings to the constraints on these physical parameters when complemented with the existing multiwavelength data from HST, Spitzer, and Herschel. We make a comparative study of different combinations of photometry and analyze how JWST improves on those values. For each of the physical quantity, say P, we define the ratio of estimated ($P^{\rm CIGALE}$) and true value ($P^{\rm input}$) as

$$Q_{\log P} = \log\left(\frac{P^{\rm CIGALE}}{P^{\rm input}}\right). \quad (1)$$

We plot this ratio as a function of the true value. Moreover, we plot the histogram of this ratio. For each of the recovered physical properties, the median value along with the 1σ dispersion is reported in Table 3. Moreover, the median and rms values of $Q_{\log P}$ for the different band combinations are explicitly reported in Table 4.

As far as the best-fit SED is concerned, we get a median reduced χ^2 value of ∼0.9–1.08 for JWST and JWST+HST photometry, but when adding FIR photometry, the value increases to ≈5. The increase in reduced χ^2 when adding Spitzer and Herschel photometry to JWST and HST data in CIGALE betrays the fact that the UV-NIR and the FIR/submillimeter bands preferentially see the emission from low- and high-obscuration regions, respectively. Also, while the JWST and the HST photometry are high resolution and well matched in aperture, the FIR/submillimeter data have larger beam sizes and potential blending issues. Our model does not allow us to deal with these issues because it yields a single, spatially integrated SED for each source, i.e., the UV/NIR and FIR/submillimeter emission are colocated by construction.

CIGALE enforces energy balance between absorbed stellar light and dust reemission. If the UV/optical fit suggests low dust attenuation, the model may struggle to match the observed IR fluxes, especially when the FIR SED shape or amplitude deviates from the assumed templates. Despite this higher reduced χ^2, the uncertainties (dispersions) in key physical parameters like stellar mass and SFR, which are the main focus of our study, remain low. This indicates that, while the exact SED shape may not be perfectly reproduced across all bands, the overall physical interpretation is robust.

4.2.1. Stellar Mass

The scatter plots of the logarithm of the ratio between the estimated stellar mass ($M_{\star}^{\rm CIGALE}$) and the input stellar mass ($M_{\star}^{\rm input}$) as a function of $M_{\star}^{\rm input}$ for the parent and the DSFG sample are shown in Figures 4 and 5, respectively. The points are color coded with their values of $|\Delta z|/(1 + z_{\rm input})$. The histogram of $Q_{\log(M_{\star})}$ is also shown in the figures. When the stellar mass is derived from the JWST photometry alone, the 1σ dispersions in $Q_{\log(M_{\star})}$ are 0.2 and 0.14 for the parent catalog and DSFG sample, respectively. CIGALE leans toward

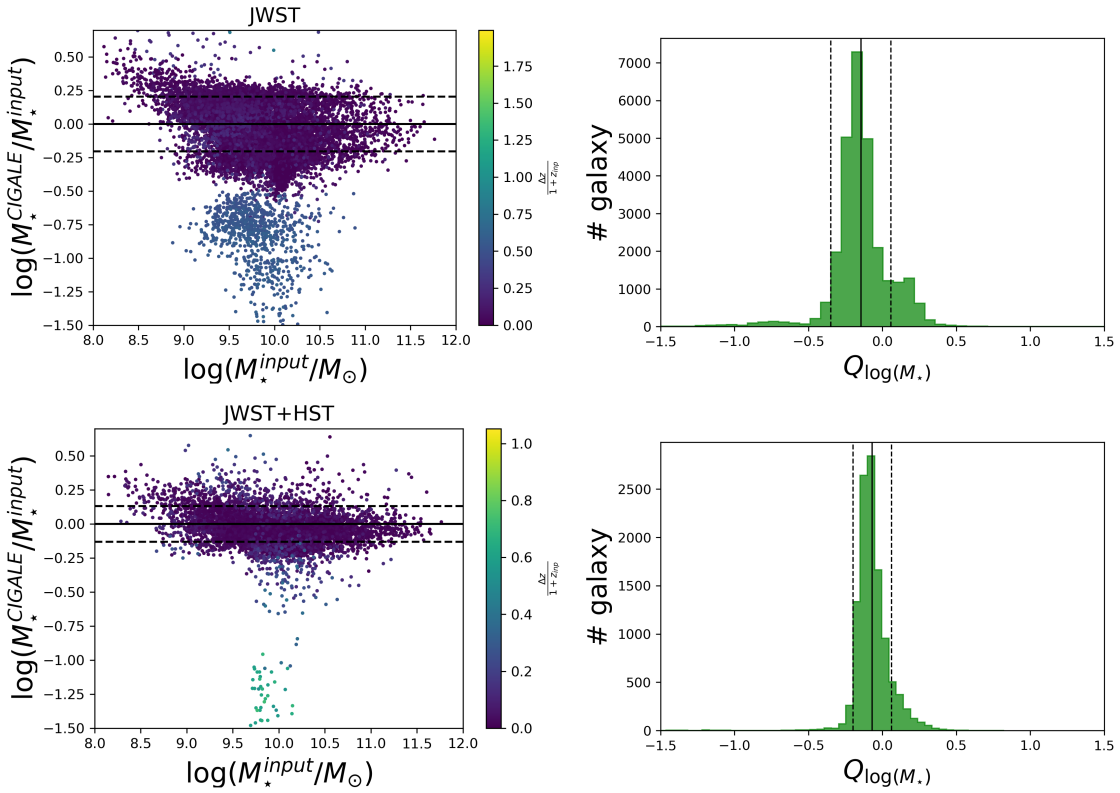

Figure 4. Scatter plot of the logarithm of the ratio between the estimated stellar mass ($M_\star^{\rm CIGALE}$) and the input stellar mass ($M_\star^{\rm input}$) as a function of $M_\star^{\rm input}$ for the parent sample of galaxies (i.e., $\log(M_{\rm vir}/M_\odot) \geqslant 11.3$) from the JWST photometry (top row) and the JWST+HST photometry (bottom row). The points are color coded with their values of $|\Delta z|/(1+z_{\rm input})$. The solid black line marks the locus of equality between the model values and the CIGALE estimated values. The boundaries of the 1σ dispersion around the mean are shown by the black dashed lines. The histograms of $Q_{\log(M_\star)}$ are shown in the right-hand panels. The black solid line marks the mean value while the dashed lines denote the 1σ dispersion around the mean. Overall, CIGALE leans toward a slight but significant systematic underestimate of the stellar mass. In the top left panel, the small dark blue patch of sources having $\log(M_\star^{\rm CIGALE}/M_\star^{\rm input}) < -0.5$ and $9 \leqslant \log(M_\star^{\rm input}/M_\odot) \leqslant 11$ is due to the sources that are AGN dominated and have catastrophic photo-z estimation errors ($|\Delta z|/(1+z_{\rm input}) \gtrsim 0.5$) by EAZY. Similarly, such outliers are present in the bottom left panel seen as yellowish green patch ($|\Delta z|/(1+z_{\rm input}) \gtrsim 0.6$) with $\log(M_\star^{\rm CIGALE}/M_\star^{\rm input}) < -1$ and $9.5 \leqslant \log(M_\star^{\rm input}/M_\odot) \leqslant 10.5$.

a slight but significant systematic underestimate of the stellar mass. Moreover, when using an exponentially declining SFH, stellar masses are often underestimated as was found by J. Pforr et al. (2012) while performing SED fitting on the semianalytic model galaxies in cosmological simulations (S. Hatton et al. 2003).

We obtain the mean of $Q_{\log(M_\star)}$ as -0.14 and -0.004 with JWST photometry for the parent and the DSFG sample, respectively. We observe that the 1σ dispersions reduce to 0.15 for the parent sample and 0.1 for the DSFG sample for removing the catastrophic photo-z outliers (AGN-dominated sources or power-law-like SEDs). Besides, the mean differences also reduce to -0.12 for the parent sample. As shown in Figure 6 (top panel) for the parent sample, including HST photometry alongside JWST leads to a noticeable reduction in both the bias and scatter of stellar mass estimates, underscoring the value of extended NIR coverage in improving SED fitting accuracy. Combining the JWST with the HST photometry, the 1σ dispersion in $Q_{\log(M_\star)}$ reduces to 0.14 for the parent sample, which after removal of outliers further decreases to 0.1. The mean difference becomes -0.068 and -0.063, respectively. This clearly shows that the dispersion in the stellar mass estimates is mainly due to the uncertainty in the photo-z. However, the overall estimation of stellar mass can be also affected by the difference in the slope of the dust attenuation law of the birth clouds (BCs) used in CIGALE and the one used in our SED formalism (D. Mitra et al. 2024). Besides, the assumed SFH and its parameterization also affect the estimation of stellar mass as pointed out by M. J. Michałowski et al. (2012) and S. Lower et al. (2020).

Moreover, for the DSFG sample, the 1σ dispersion reduces to 0.1 upon adding HST photometry to that of JWST. The mean offset is 0.035. Adding HST photometry in the F435W and F160W bands to JWST/NIRCam data significantly improves the accuracy of stellar mass estimates by reducing key degeneracies in the SED fitting process. The F435W filter probes the rest-frame ultraviolet at redshifts $z \sim 1.5$–3, providing sensitivity to recent star formation and dust attenuation. This helps constrain the contribution of young stellar populations and mitigates the age–dust degeneracy that can otherwise bias mass estimates. The F160W filter, on the other hand, samples the rest-frame optical light and is crucial for capturing features like the Balmer and 4000 Å breaks, which are strong indicators of older stellar populations that dominate the total stellar mass. Together, these two HST bands fill important gaps in wavelength coverage and complement the longer-wavelength NIRCam filters by anchoring both the blue and red ends of the SED. As a result, the stellar population properties—particularly the mass-to-light ratio—

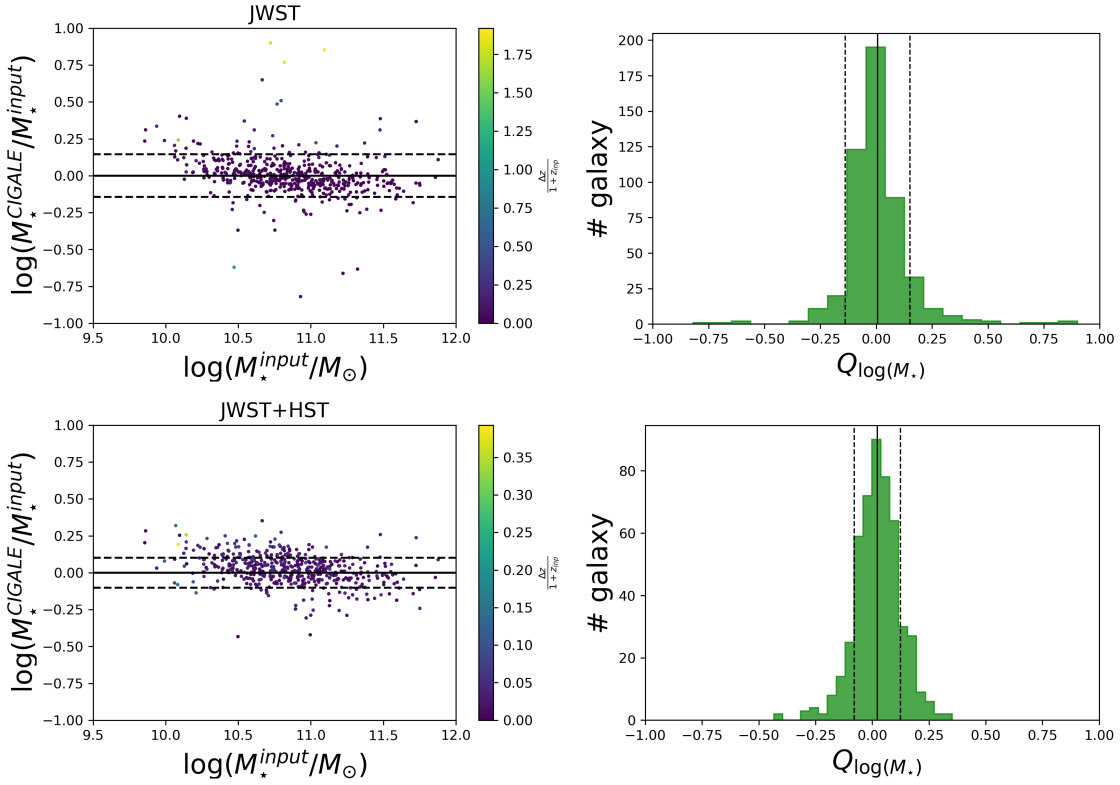

Figure 5. Scatter plot of the logarithm of the ratio of estimated stellar mass ($M_\star^{\rm CIGALE}$) and the input stellar mass ($M_\star^{\rm input}$) as a function of $M_\star^{\rm input}$ for the DSFG sample from the JWST photometry (top row) and the JWST+HST photometry (bottom row). The points are color coded with their values of $|\Delta z|/(1+z_{\rm input})$. The histograms of $Q_{\log(M_\star)}$ are shown in the right-hand panels. The meanings of the different line styles are the same as in Figure 4.

are better constrained, leading to a measurable reduction in the 1σ dispersion of stellar mass estimates.

For the subsample, we also considered different combinations of photometry to estimate the stellar mass. The estimated stellar masses derived from the photometry from HST, Spitzer, and Herschel have mean and median deviations from the true values of 0.01 and 0.23 in $Q_{\log(M_\star)}$. An rms value and a mean value of 0.16 and -0.13 are obtained when using JWST +Spitzer+Herschel photometry. Estimating the stellar mass from HST+JWST+Spitzer+Herschel photometry also gave a 1σ dispersion of 0.15 and a mean offset of -0.04. Figure 6 (bottom panel) shows the recovery of the stellar mass for the DSFG subsample using various photometric combinations. JWST/NIRCam photometry alone yields minimal bias and low scatter, highlighting its strength in constraining stellar mass. Adding HST data does not significantly improve the estimates and introduces a slight positive bias. Legacy IR data without JWST result in larger scatter, while including JWST improves accuracy. As the evolved stellar populations dominate the stellar mass of galaxies and have most of their emission in the rest-frame optical/NIR, the addition of FIR photometry does not significantly improve the constraints on the stellar mass estimate. These findings underscore the remarkable capability of JWST in recovering the stellar mass of DSFGs.

4.2.2. SFR

The SFR of dust-enshrouded objects cannot be traced accurately using only the NIR photometry (J. Pforr et al. 2012, 2013; Euclid Collaboration 2023; D. Mitra et al. 2024). In estimating the SFR, $\dot{M}_\star$, from JWST photometry, we obtain 1σ dispersions of $\approx$0.8 and 0.55 in $Q_{\log(\dot{M}_\star)}$ for the parent sample and subsample, respectively; the mean offsets are 0.14 and -0.05, respectively. Adding the HST to JWST photometry, the 1σ dispersions reduce, but are still high with values of 0.36 and 0.47 for the two samples, respectively. The mean differences are -0.044 and -0.019. Therefore, complementing the JWST and/or the HST photometry with photometric data from FIR bands is crucial for estimating the SFR.

We now give estimates of SFR for different combinations of photometry for the DSFG sample only. For comparison, we also calculate the SFR from the FIR photometry alone. The mean and the 1σ dispersion of $Q_{\log(\dot{M}_\star)}$ are -0.196 and 0.22 for the Spitzer plus Herschel photometry. Adding the HST photometry to the above improves the estimation with the 1σ dispersion being 0.169, and the mean reduces to 0.037. Figure 7 shows the scatter plot of the logarithm of the ratio of estimated ($\dot{M}_\star^{\rm CIGALE}$) to input SFR ($\dot{M}_\star^{\rm input}$), color coded with the values of $|\Delta z|/(1+z_{\rm input})$. Also shown are the histogram of the ratio $Q_{\log(\dot{M}_\star)}$. Upon replacing HST with JWST in the above combination, we get a 1σ dispersion of 0.16 and a mean of 0.044. However, when combining all the photometry from JWST+HST+Spitzer+Herschel, the dispersion increases to 0.18, and the mean becomes 0.053.

The HST F435W and F160W filters sample the rest-frame UV and optical light at high redshift, which trace only the unobscured star formation. In DSFGs, this component is heavily suppressed and variable, leading to increased

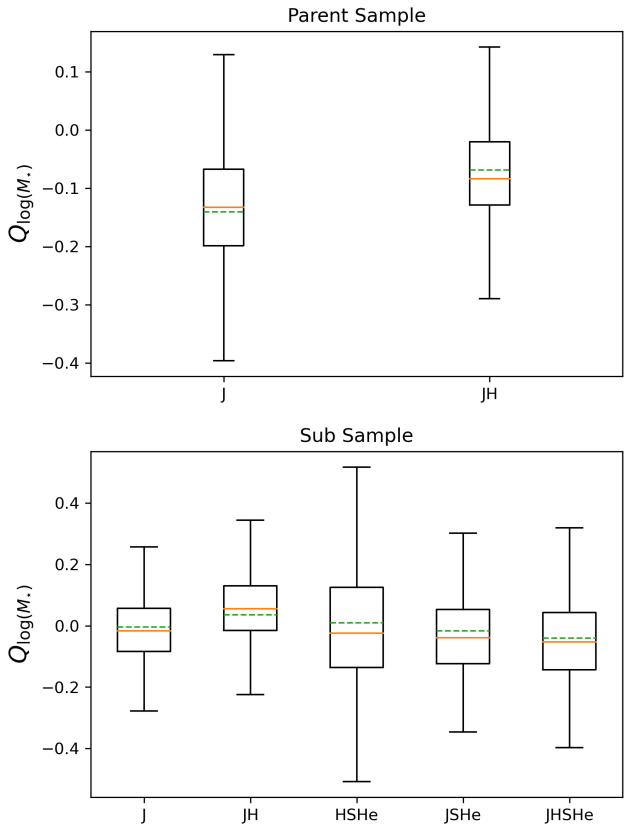

Figure 6. Boxplot showing the distribution of the $Q_{\log(M_\star)}$, for the parent sample (top panel) using JWST and JWST+HST photometry and the DSFG sample (bottom panel) using JWST, JWST+HST, JWST+Spitzer+Herschel, and JWST+HST+Spitzer+Herschel photometry. The solid orange line denotes the median, while the dashed green line represents the mean. The interquartile range and whiskers indicate the spread and outliers of the distribution. Here, the abbreviations in the labels are: J (JWST), JH (JWST +HST), JSHe (JWST+Spitzer+Herschel), and JHSHe (JWST+HST+Spitzer +Herschel).

uncertainties and degeneracies in CIGALE's energy balance when fitting both obscured and unobscured SFR components —thereby increasing the dispersion in total SFR estimates. Moreover, this increase in the dispersion can also be due to the presence of some photo-z outliers in the sample.

A slight offset between the SFRs by CIGALE and the true values is expected, due to the different dust attenuation law slopes adopted by CIGALE and by E. da Cunha et al. (2008). However, our results show that the effect is minor. Figure 8 presents the accuracy of SFR recovery for the DSFG subsample using different combinations of photometric bands. The results show that using only Spitzer and Herschel data leads to higher dispersion and a slight underestimation of SFRs (we recall that, in most cases, we have Herschel photometry only at 250 μm). The inclusion of JWST photometry significantly improves the estimates, reducing both bias and scatter. Adding HST data provides minimal additional benefit and may slightly worsen the results, likely due to the limited utility of rest-frame UV data in dust-obscured galaxies. Overall, these findings emphasize the crucial role of JWST in accurately constraining the SFRs of DSFGs.

Given that these galaxies are IR bright and dusty, the availability of robust FIR/submillimeter data plays a vital role in the estimation of the SFR. Restricting the analysis of the SFR to the 33% sources from the DSFG sample detected by Spitzer+Herschel at $>5\sigma$ in all Spitzer/MIPS and Herschel (PACS and SPIRE) bands gives a 1σ dispersion of 0.14, 0.13, and 0.15, respectively, in $Q_{\log(M_\star)}$ for Spitzer +Herschel, JWST+Spitzer+Herschel, and JWST+HST +Spitzer+Herschel photometry. Similarly, the 1σ dispersions in $Q_{\log(M_{\star,10})}$ for these $>5\sigma$ detected sources are 0.12, 0.12, and 0.15, respectively, for the same photometry combinations. Overall, we find that the SFR estimation was very challenging since it is very sensitive to the SFH (S. Lower et al. 2020). To verify this, we performed a test by keeping all the parameters of CIGALE unchanged and changing the assumed SFH from `sfhdelayed` to `sfhdelayedbq`.[4] Using `sfhdelayedbq` to estimate SFR, we found that SFR is underestimated almost by an order of magnitude. When switching from `sfhdelayed` to `sfhdelayedbq` in CIGALE, the model allows for a recent burst or quenching event. For DSFGs, which typically have high, sustained SFRs, the burst/quench parameters can cause the fit to interpret their IR-luminous phase as a postburst decline, leading to underestimated current SFRs. This misinterpretation happens because `sfhdelayedbq` may assign much of the star formation to an earlier burst, reducing the inferred ongoing SFR compared to the smoother `sfhdelayed` model. L. K. Hunt et al. (2019) argued that, due to the sensitive nature of SFR to SFH, certain SED fitting algorithms may find it difficult to determine the most appropriate SFH due to degeneracies. Consequently, a range of different SFHs may yield comparably good SED fits.

4.2.3. Dust Luminosity and Dust Mass

The dust luminosity and the dust mass of our simulated DSFGs are computed using different combinations of photometric data: Spitzer+Herschel, HST+Spitzer+Herschel, JWST+Spitzer+Herschel, and JWST+HST+Spitzer+Herschel. Figure 9 shows the distribution of $\log(L_{\rm dust}^{\rm CIGALE}/L_{\rm dust}^{\rm input})$ as a function of input $L_{\rm dust}$ along with the histogram of $Q_{\log(L_{\rm dust})}$. With all the different combinations of photometry, we could recover the dust luminosity quite accurately with the 1σ dispersion in $Q_{\log(L_{\rm dust})}$ being the least for JWST+Spitzer+Herschel, with a value of 0.12. The mean offset in this case is -0.049. Upon adding the HST data to the above, the 1σ dispersion increases to 0.13 due to the photo-z outliers, and the mean offset becomes -0.066. Combining only HST data with FIR photometry, we get the dispersion value of 0.13 and a mean value of -0.06. Only Spitzer+Herschel produces a mean value of 0.075 and a dispersion of 0.15. Overall, we observe that, upon adding UV/optical/NIR photometry, the dust extinction is better constrained, thus giving a more accurate estimate of $L_{\rm dust}$ as summarized in Figure 10 (top panel). From the values of the estimated median dust luminosity (see Table 3), we can categorize these galaxies as ultraluminous infrared galaxies.

The distribution of $\log(M_{\rm dust}^{\rm CIGALE}/M_{\rm dust}^{\rm input})$ as a function of input $M_{\rm dust}$ along with the histogram of $Q_{\log(M_{\rm dust})}$ is shown in Figure 11. The dust mass estimation has a larger dispersion

[4] The `sfhdelayed` module models a smooth, rising-and-declining SFH, while `sfhdelayedbq` extends this by allowing for a recent burst or quenching event, making it more suitable for galaxies with abrupt SFR changes.

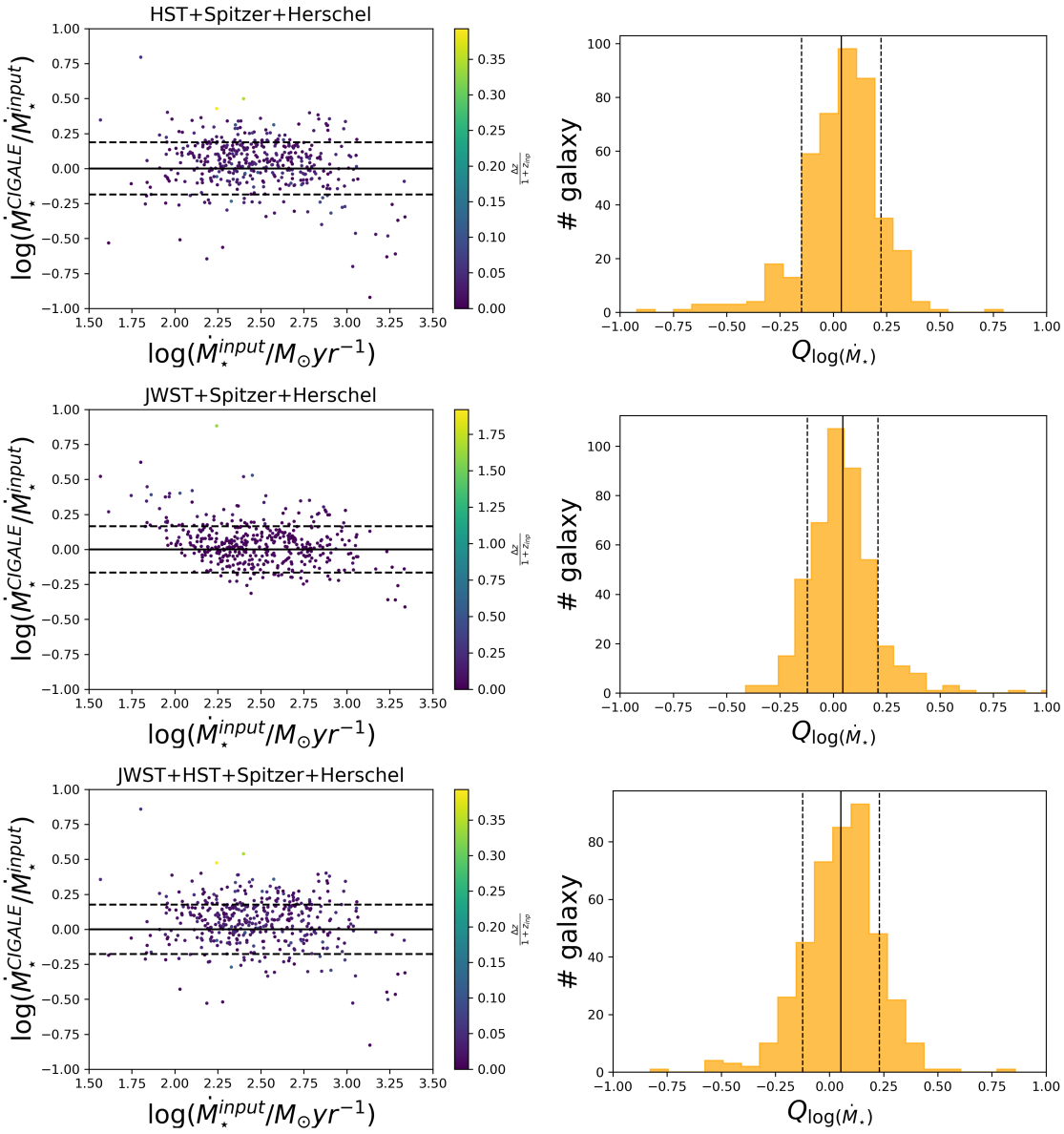

Figure 7. Scatter plot of the logarithm of the ratio of estimated ($\dot{M}_\star^{\rm CIGALE}$) to input ($\dot{M}_\star^{\rm input}$) SFR obtained for the DSFG sample from HST+Spitzer+Herschel, JWST +Spitzer+Herschel, and JWST+HST+Spitzer+Herschel photometry. The points are color coded with their values of $|\Delta z|/(1+z_{\rm input})$. The histogram of $Q_{\log(\dot{M}_\star)}$ is also shown in the figures The meaning of the different line styles is the same as in Figure 4.

compared to the dust luminosity (see Figure 10, bottom panel). The 1σ dispersions in $Q_{\log(M_{\rm dust})}$ are 0.29, 0.27, 0.26, and 0.28 for the Spitzer+Herschel, HST+Spitzer+Herschel, JWST +Spitzer+Herschel, and JWST+HST+Spitzer+Herschel photometry, respectively, while the mean offsets are −0.012, 0.124, 0.150, 0.130. Overall, CIGALE gives an overestimation of dust mass that can be due to the difference in the value of the reference emissivity of dust grains per unit of mass, κ_0, adopted by the two SED fitting codes (C.-L. Liao et al. 2024). Moreover, L. K. Hunt et al. (2019) while comparing various SED fitting models by fitting far-UV to submillimeter photometry data of 61 KINGFISH galaxies found that CIGALE overestimates $M_{\rm dust}$ as compared to MAGPHYS (based on E. da Cunha et al. 2008 SED formalism) due to the absence of an agreement regarding dust opacity.

Also, from Figure 11, it is observed that there is a negative correlation between $\log(M_{\rm dust}^{\rm CIGALE}/M_{\rm dust}^{\rm input})$ and $\log(M_{\rm dust}^{\rm input})$. This negative correlation is likely due to the assumption of fixed dust absorption coefficient (κ) and emissivity index (β) by CIGALE. S. Bianchi et al. (2022) pointed out the need for more realistic dust emission models that consider the temperature distribution and varying dust opacity across different environments. We note that the discrepancy between $M_{\rm dust}^{\rm CIGALE}$ and $M_{\rm dust}^{\rm input}$ is more prominent for $\log(M_{\rm dust}^{\rm input}) \lesssim 8.5$, where CIGALE substantially overestimates $M_{\rm dust}$. For $\log(M_{\rm dust}^{\rm input}) \gtrsim 9$, the negative correlation is not significant. To further explore this effect, we performed a test comparing the logarithmic ratios of dust mass and dust temperature estimated by CIGALE to those from our model. Our model uses a three-component dust temperature to calculate the dust mass whereas CIGALE models the dust emission using a

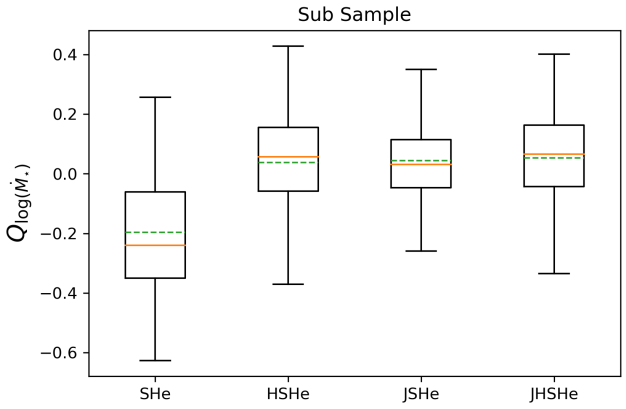

Figure 8. Boxplot showing the distribution of the $Q_{\log(\dot{M}_\star)}$ for the DSFG sample using HST+Spitzer+Herschel (HSHe), JWST+Spitzer+Herschel (JSHe), and JWST+HST+Spitzer+Herschel (JHSHe) photometry. The solid orange line denotes the median, and the dashed green line indicates the mean. The interquartile range and whiskers indicate the spread and outliers of the distribution.

range of interstellar radiation field intensities (U). To define a single dust temperature from our model, we calculate the mass-weighted dust temperature as

$$T_{\rm dust}^{\rm inp} = \frac{(M_{\rm dust,W}^{\rm BC} T_{w,\rm BC} + M_{\rm dust,W}^{\rm ISM} T_{w,\rm ISM} + M_{\rm dust,c}^{\rm ISM} T_{c,\rm ISM})}{(M_{\rm dust,W}^{\rm BC} + M_{\rm dust,W}^{\rm ISM} + M_{\rm dust,c}^{\rm ISM})}. \quad (2)$$

For more details about the model calculation of dust mass and the meanings of the above symbols, we refer the readers to D. Mitra et al. (2024). To calculate the dust temperature estimated by CIGALE, we use the best-fit mean intensity $U_{\rm mean}$ in the relation from B. T. Draine et al. (2014)

$$T_{\rm dust}^{\rm CIGALE} = 18 U_{\rm mean}^{\frac{1}{6}}. \quad (3)$$

We then compute $Q_{\log(T_{\rm dust})} = \log(T_{\rm dust}^{\rm CIGALE}/T_{\rm dust}^{\rm inp})$ and compute its correlation with $Q_{\log(M_{\rm dust})}$. We observe a clear negative correlation between $Q_{\log(M_{\rm dust})}$ and $Q_{\log(T_{\rm dust})}$ as shown in Figure 12, consistent with the known degeneracy in SED fitting. This anticorrelation indicates that, when CIGALE infers a higher dust temperature relative to our model, it tends to infer a lower dust mass, and vice versa. This is because, for a given FIR luminosity, higher temperatures require less dust to produce the same emission, and models must compensate accordingly. This trend highlights that differences in dust temperature assumptions can significantly impact the inferred dust masses, even when the overall FIR luminosities are matched.

The estimated dust mass from the different photometry combinations of our simulated sources has a median value of $\log(M_{\rm dust}/M_\odot) \gtrsim 8.5$. Similar dust mass estimates were obtained by E. da Cunha et al. (2015) while studying with ALMA a sample of 122 870 μm detected sources in the Extended Chandra Deep Field South. A. M. Swinbank et al. (2014) also reported dust mass estimates consistent with ours while studying the FIR properties of a sample of 99 SMGs in the Extended Chandra Deep Field South at 870 μm with ALMA. In general, these galaxies have a higher dust content than the low-z ($z < 1$) galaxies, as was shown by K. Rowlands et al. (2014).

4.3. Comparison with Physical Properties of DSFG Sources in the ASTRODEEP-JWST Catalog

To enable a realistic comparison between observed and simulated DSFGs, we constructed a catalog of DSFG counterparts based on the ASTRODEEP-JWST photometric catalog by applying NIR color selection criteria optimized for identifying dusty galaxies, following the method described by A. J. Barger & L. L. Cowie (2023). These criteria are tailored to select DSFGs using only NIRCam bands, providing a practical strategy for identifying heavily dust-obscured galaxies in JWST surveys where FIR data may be limited. In parallel, we applied the same selection criteria to our simulated DSFG subsample to generate a corresponding mock catalog that mimics the observational selection. For both the observed and simulated samples, we performed SED fitting using CIGALE, incorporating the same model assumptions and wavelength coverage, in order to derive physical parameters such as stellar mass and SFR. This procedure ensures a fair comparison between the simulated and observed populations under identical selection and fitting conditions, allowing us to assess the reliability of our modeling framework in reproducing the physical properties of JWST-selected DSFGs.

The ASTRODEEP-JWST catalog provides photometric redshift estimates using EAZY and ZPHOT (A. Fontana et al. 2000) based on JWST NIRCam and HST photometry for sources in six extragalactic deep fields including GOODS-S, aimed at studying the high-redshift Universe. The catalog comprises all sources detected at 5σ in the NIRCam F444W band. The GOODS-S catalog consists of 73,638 sources in the redshift range $0 \leqslant z \leqslant 20$. As our simulations are limited to the range $1 \leqslant z \leqslant 8$ (for more details, see D. Mitra et al. 2024), we considered only the 55,028 ASTRODEEP sources within this range.

The NIRCam A. J. Barger & L. L. Cowie (2023) photometric criteria for selecting DSFG are defined as follows:

$$S_{\rm F444W}/S_{\rm F150W} > 3.5,\ S_{\rm F444W} > 1\ \mu{\rm Jy}. \quad (4)$$

By applying the above selection criteria to both the ASTRODEEP-JWST catalog and the simulated sample, we create a sample of NIRCam DSFGs having 866 and 516 galaxies, respectively. This color selection along with the distribution of sources both in the ASTRODEEP-JWST catalog and the simulated sample is shown in Figure 13.

For the estimation of physical properties of the ASTRODEEP NIRCam DSFGs sources, we used the same modules of CIGALE specified in Section 3.3. For these ASTRODEEP sources, the estimated stellar mass and SFR have a median value of $\log(M_\star/M_\odot) = 10.12 \pm 0.3$ and $\log(\dot{M}_\star/M_\odot yr^{-1}) = 2.4 \pm 0.4$, respectively. For the simulated NIRCam DSFGs, the estimated stellar mass and SFR have a median value of $\log(M_\star/M_\odot) = 10.3 \pm 0.3$ and $\log(\dot{M}_\star/M_\odot yr^{-1}) = 2.0 \pm 0.3$, respectively.

Figure 14 shows the histograms of stellar masses and SFRs of both the ASTRODEEP and the simulated DSFGs as a function of redshift. The distributions of the stellar mass and SFR for the ASTRODEEP and the simulated sources are in good agreement. This overall agreement between the simulated DSFG sample and the NIRCam-selected DSFGs from the ASTRODEEP catalog highlights the consistency of the simulation framework with observational data. Furthermore,

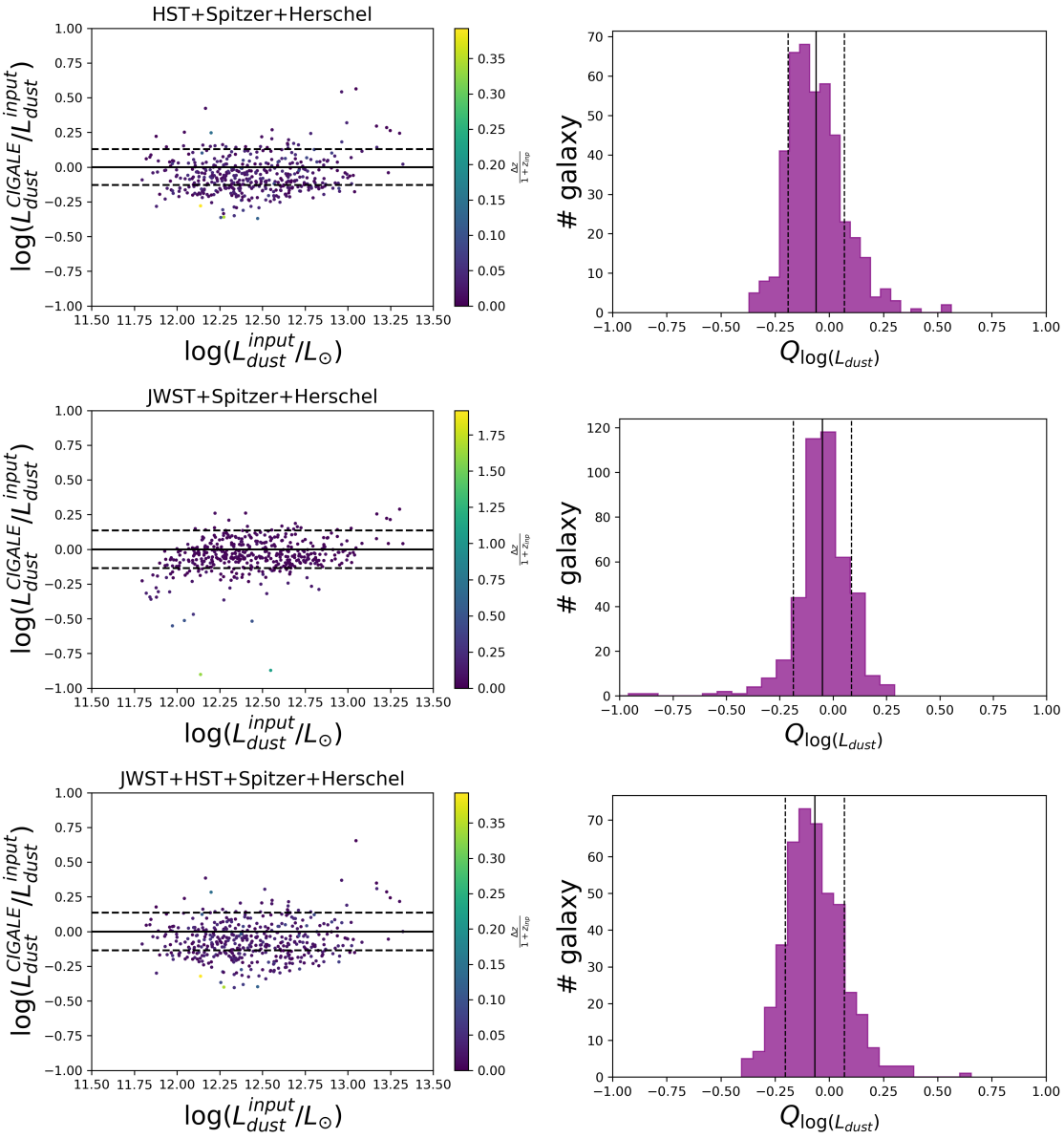

Figure 9. Same as Figure 7, but for the dust luminosity ($L_{\rm dust}$).

this comparison underscores the efficacy of JWST in detecting DSFGs with stellar masses as low as $\sim 10^{10} M_{\odot}$.

5. Summary and Conclusions

We have investigated the ability of the JWST to study the properties of $z > 1.5$ progenitors of present-day massive spheroidal galaxies, using the JADES survey strategy in the GOODS-S field. We also analyzed the effect of complementing JWST data with the data from previous surveys with HST, Spitzer, and Herschel. Our analysis is based on the physical model by Z.-Y. Cai et al. (2013) for the evolution of protospheroidal galaxies, as upgraded by D. Mitra et al. (2024). We have found that our model is consistent with the recent observations of MIR LFs of these high-z galaxies.

Using the model, we simulated a sample of protospheroidal galaxies, which we called the parent sample, with $\log(M_{\rm vir}/M_{\odot}) \gtrsim 11.3$ and $z \geqslant 1.5$, over a survey area of 87.5 arcmin^2, similar to the area covered by JADES-Medium in the GOODS-S field. According to the model, at the 5σ detection limit in the nine NIRCam filters chosen for JADES, JWST detects 27,748 galaxies of which about 41% are also detected by HST above 5σ in the F435W and F160W bands. In this sample, only about $\sim$2% of the JWST sources are detected at $>5\sigma$ by Spitzer and Herschel. So, to include the photometry from the above IR instruments, we focused on the subsample of galaxies with $\log(M_{\rm vir}/M_{\odot}) \gtrsim 12$, as Herschel did not detect DSFGs below that threshold anyway. From this subsample, we constructed a DSFG sample by selecting galaxies that are detected at $\geqslant 5\sigma$ at 250 μm with Herschel. This yielded 507 simulated dusty galaxies. Among these, 503 galaxies ($\sim$99%) are also detected at 5σ in all nine NIRCam bands, and approximately 98.8% are detected by HST. Furthermore, 434 galaxies ($\sim$86%) in this DSFG sample are simultaneously detected at $>5\sigma$ in both Spitzer/MIPS bands.

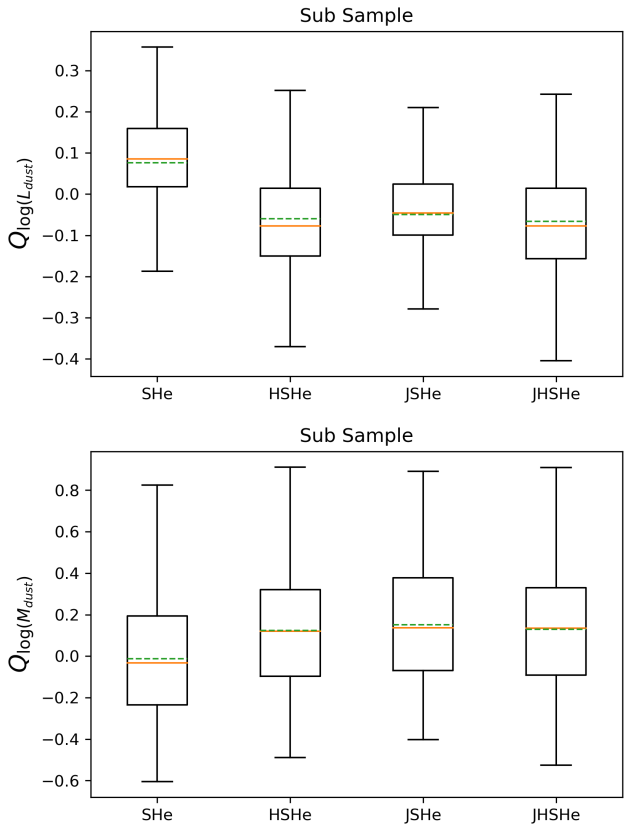

Figure 10. Same as Figure 8, but for the dust luminosity ($L_{\rm dust}$, top panel) and dust mass ($M_{\rm dust}$, bottom panel).

The first thing we estimated for our simulated DSFGs was the photometric redshift. For that, we used EAZY on the JWST photometry alone as well as on the JWST+HST photometry. Then, we estimated the physical properties using the code CIGALE and different combinations of photometric data: JWST, JWST+HST, Spitzer+Herschel, HST+Spitzer +Herschel, JWST+Spitzer+Herschel, and JWST+HST +Spitzer+Herschel. Our findings are as follows

1. We found that, for 90% of the sources detected by JWST at 5σ, EAZY gave a good estimate of the photometric redshift with the accuracy in $(1+z)$ being better than 15%. Catastrophic outliers in the $4 \leqslant z \leqslant 6$ range were mostly due to the degeneracy between the Lyman break and the 4000 break. Upon addition of the HST photometry to the JWST data, most catastrophic outliers were removed; in fact, by adding filters blueward of 0.7 μm, the Lyman break could be properly sampled. We got a more accurate estimate of redshift, with $<$15% discrepancy in (1+z) for $\gtrsim$98% sources detected by both JWST and HST. Catastrophic error estimates are then limited to the 1%–2% AGN-dominated sources. For the DSFG sample, JWST provided estimates of the photometric redshift with the accuracy in $(1+z)$ being better than 15% for $\gtrsim$95% sources, which further increased to $\sim$99% upon adding HST photometry.
2. Using the JWST photometry alone, $\log(M_\star^{\rm CIGALE}/M_\star^{\rm input})$ has a 1σ dispersion of $\approx$0.2 for the parent sample and 0.14 for the subsample, respectively. For removing the photo-z outliers, the 1σ dispersion reduces to $\approx$0.15 and 0.1, respectively. This clearly shows the direct effect of wrong photo-z estimation on the estimation of stellar mass. As expected, adding the submillimeter photometry from Spitzer and Herschel produced little improvement on the stellar mass estimate. Adding the HST photometry to that of JWST, the stellar mass could be recovered relatively well with a 1σ dispersion as low as 0.14 for the parent sample and 0.1 for the subsample; also, the mean offset between true and estimated stellar masses decreases. This shows that, as expected, the stellar mass is more sensitive to rest-frame UV/optical/NIR wavelengths than to the FIR/submillimeter part of the SED.
3. The SFR cannot be accurately derived from the JWST photometry alone: the rms dispersion of $Q_{\log(\dot{M}_\star)} = \log(\dot{M}_\star^{\rm CIGALE}/\dot{M}_\star^{\rm input})$ is 0.55. The addition of the HST photometry leads to a modest improvement, but the dispersion remains high. Only FIR/submillimeter data from Spitzer/MIPS and Herschel (PACS and SPIRE) allowed us to decrease the dispersion in $Q_{\log(\dot{M}_\star)}$ to 0.16–0.18. As expected, the availability of robust FIR/submillimeter photometry is crucial for constraining the SFR accurately. Unfortunately, these data are available only for a tiny fraction of the sample. On the other hand, we found that the FIR/submillimeter photometry alone yields a dispersion of 0.22, demonstrating that the addition of JWST data significantly improves the accuracy. On the whole, the sampled sources have a median SFR $\log(\dot{M}_\star/M_\odot\ {\rm yr}^{-1}) \sim 2.5$, clearly showing that these galaxies are going through intense star formation activity.
4. Dust luminosity and dust mass could only be estimated for sources having Spitzer and Herschel photometry. The estimated dust luminosity has a median value of $\log(L_{\rm dust}/L_\odot) \sim 12.5$, while the median value of the estimated dust mass is $\log(M_{\rm dust}/M_\odot) \sim 8.5$, showing that these DSFGs at $z \gtrsim 1.5$ are highly luminous and are more heavily dust-enshrouded than $z \sim 1$ galaxies. Again, the addition of JWST data improves the accuracy. Estimates of dust masses are affected by the substantial uncertainty of the value of the reference emissivity of dust grains per unit of mass. It is also affected by dust temperature assumptions.
5. Our estimates of the stellar mass and SFR for the ASTRODEEP-JWST sources demonstrate the capability of JWST to detect high-z galaxies with a stellar mass almost an order of magnitude lower than possible in the pre-JWST era. The comparison of the estimated physical properties of the ASTRODEEP sources and our simulated sources shows a good level of consistency between the two.

Therefore, in this work, we have shown that, in the GOODS-S field, JWST alone can well constrain the stellar mass of massive DSFGs. The estimates of the physical properties of DSFGs can be improved by exploiting the rich HST, Spitzer, and Herschel data available from previous surveys like CANDELS. To recover the IR properties of DSFGs, the JWST and HST data should be complemented with those from Spitzer and Herschel; however, deeper FIR/submillimeter data are badly needed. Overall, it can be concluded that JWST can enrich the study of DSFGs by producing tighter constraints on the physical properties and

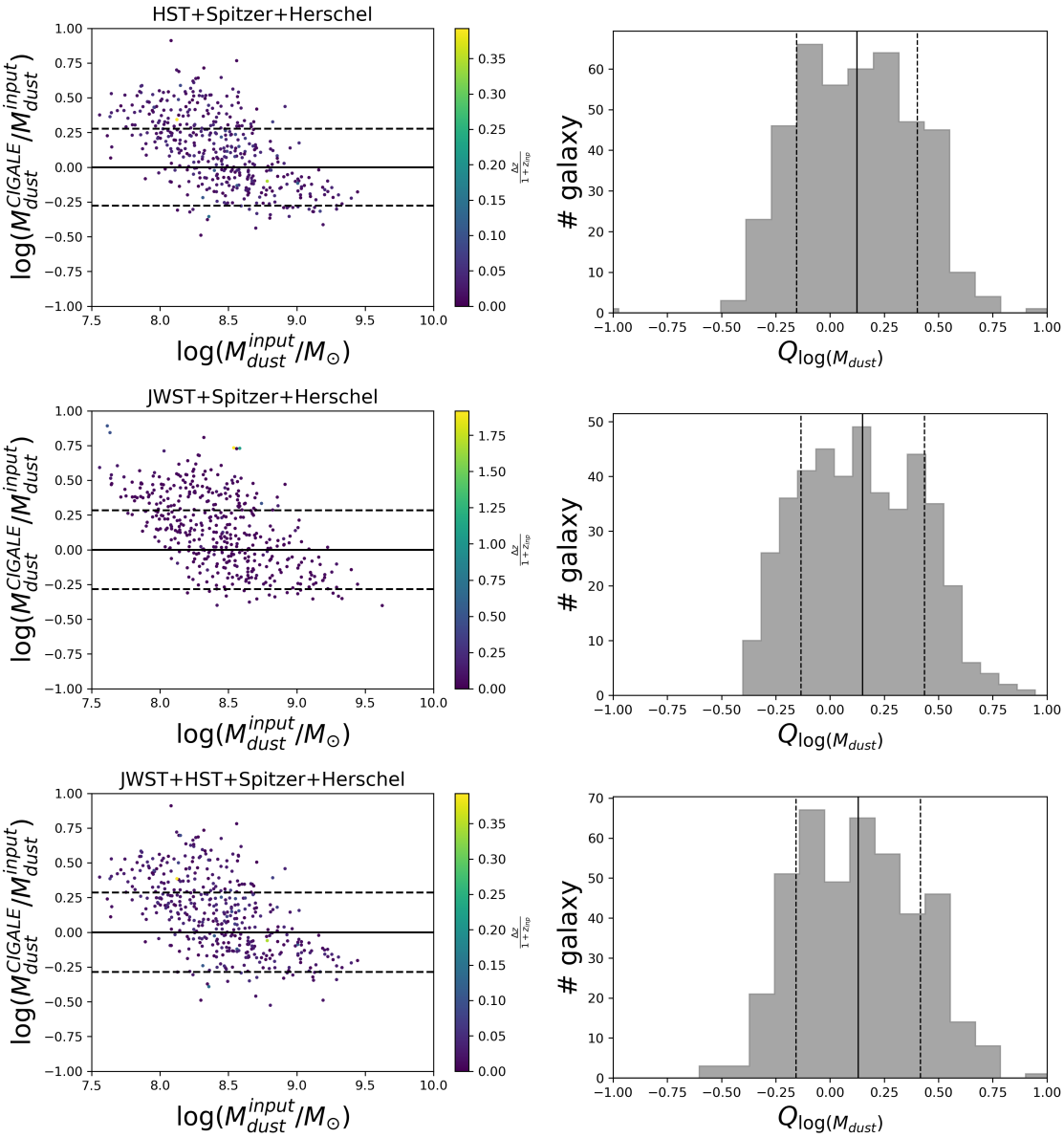

Figure 11. Same as Figure 7, but for the dust mass ($M_{\rm dust}$).

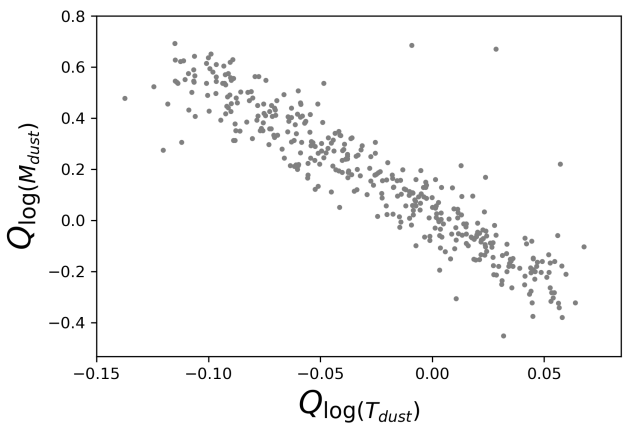

Figure 12. Scatter plot showing the correlation between $Q_{\log(M_{\rm dust})}$ and $Q_{\log(T_{\rm dust})}$. A clear negative trend is observed, highlighting the degeneracy between dust mass and dust temperature in SED fitting. This indicates that, when CIGALE estimates a higher dust temperature relative to the input model, it compensates by assigning a lower dust mass, and vice versa.

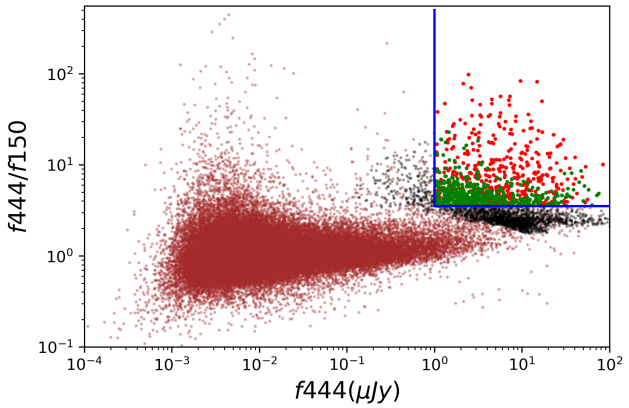

Figure 13. Colorflux diagram for NIRCam DSFG selection showing the ratio $f444/f150$ vs. $f444$ (in μJy) for galaxies in the simulated (black points) and ASTRODEEP (brown points) sample. Red points correspond to NIRCam DSFG candidates from ASTRODEEP sample, while green points represent NIRCam DSFG candidates from the simulated sample. The A. J. Barger & L. L. Cowie (2023) selection criteria is shown in blue lines.

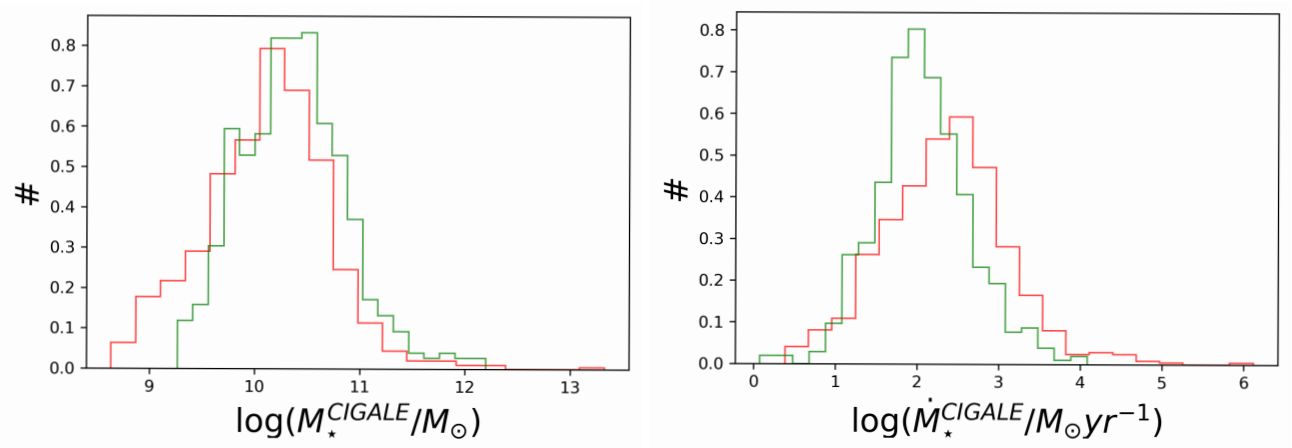

Figure 14. Normalized distribution of stellar masses (left) and SFR (right) derived from CIGALE for the simulated (green) and the ASTRODEEP (red) NIRCam-selected DSFGs.

revealing fainter, lower-mass dusty galaxies previously inaccessible to Herschel or Spitzer.

This work clearly demonstrates the transformative role of JWST in advancing our understanding of dusty galaxy populations at high redshift. Nonetheless, it also highlights the limitations imposed by the lack of sufficiently deep FIR and submillimeter observations. Future facilities such as the proposed PRIMA or next-generation ground-based submillimeter observatories will be crucial for probing the peak of dust emission and disentangling the star formation and AGN components more robustly. Continued development of sensitive, high-resolution IR probes will further complement the capabilities of JWST, enabling a more complete census of the dust-obscured Universe and enhancing our ability to trace galaxy evolution across cosmic time. A critical problem for space-borne FIR/submillimeter probes is angular resolution. A promising perspective is offered by FIR interferometry, which can achieve subarcsecond resolution (D. Leisawitz et al. 2008; M. Bonato et al. 2024).

Acknowledgments

D.M. acknowledges the postgraduate studentship provided by the UK Science and Technology Facilities Council (STFC). In this work, we have used the following Python packages: Astropy[5] (Astropy Collaboration 2013, 2018, 2022), Scipy[6] (E. Jones et al. 2001), Numpy[7] (S. van der Walt et al. 2011; C. R. Harris et al. 2020), Joblib,[8] COLOSSUS[9] (B. Diemer 2018), Seaborn[10] (M. Waskom 2021), and Matplotlib[11] (J. D. Hunter 2007). The authors would like to thank the anonymous referee for the thorough review and constructive feedback, which helped to refine the manuscript.

Author Contribution

D.M. was responsible for the analysis and modeling as well as the preparation and presentation of this manuscript. M.N. and G.D.Z. contributed to the interpretation and the overall development of the manuscript.

[5] https://www.astropy.org/
[6] https://scipy.org/index.html
[7] https://numpy.org/
[8] https://joblib.readthedocs.io/en/stable/
[9] https://pypi.org/project/colossus/
[10] https://seaborn.pydata.org/index.html
[11] https://matplotlib.org/

ORCID iDs

Mattia Negrello https://orcid.org/0000-0002-7925-7663

References

Alberts, S., Rujopakarn, W., Rieke, G. H., Jagannathan, P., & Nyland, K. 2020, ApJ, 901, 168
Amvrosiadis, A., Wardlow, J. L., Birkin, J. E., et al. 2025, MNRAS, 536, 3757
Astropy Collaboration 2013, A&A, 558, A33
Astropy Collaboration 2018, AJ, 156, 123
Astropy Collaboration 2022, ApJ, 935, 167
Barger, A. J., & Cowie, L. L. 2023, ApJ, 956, 95
Barger, A. J., Cowie, L. L., Sanders, D. B., et al. 1998, Natur, 394, 248
Barro, G., Prez-Gonzlez, P. G., Cava, A., et al. 2019, ApJS, 243, 22
Beckwith, S. V. W., Stiavelli, M., Koekemoer, A. M., et al. 2006, AJ, 132, 1729
Bernardi, M., Shankar, F., Hyde, J. B., et al. 2010, MNRAS, 404, 2087
Bianchi, S., Casasola, V., Corbelli, E., et al. 2022, A&A, 664, A187
Birkin, J. E., Puglisi, A., Swinbank, A. M., et al. 2024, MNRAS, 531, 61
Bonato, M., Leisawitz, D., De Zotti, G., et al. 2024, ApJ, 977, 208
Boquien, M., Burgarella, D., Roehlly, Y., et al. 2019, A&A, 622, A103
Brammer, G. B., van Dokkum, P. G., & Coppi, P. 2008, ApJ, 686, 1503
Bruzual, G., & Charlot, S. 2003, MNRAS, 344, 1000
Burgarella, D., Buat, V., & Iglesias-Pramo, J. 2005, MNRAS, 360, 1413
Cai, Z.-Y., Lapi, A., Xia, J.-Q., et al. 2013, ApJ, 768, 21
Chabrier, G. 2003, PASP, 115, 763
Charlot, S., & Fall, S. M. 2000, ApJ, 539, 718
da Cunha, E., Charlot, S., & Elbaz, D. 2008, MNRAS, 388, 1595
da Cunha, E., Walter, F., Smail, I. R., et al. 2015, ApJ, 806, 110
Davis, M., Guhathakurta, P., Konidaris, N. P., et al. 2007, ApJL, 660, L1
Diemer, B. 2018, ApJS, 239, 35
Draine, B. T., Aniano, G., Krause, O., et al. 2014, ApJ, 780, 172
Eales, S., Dunne, L., Clements, D., et al. 2010, PASP, 122, 499
Eisenstein, D. J., Willott, C., Alberts, S., et al. 2023, arXiv:2306.02465
Erb, D. K., Pettini, M., Shapley, A. E., et al. 2010, ApJ, 719, 1168
Euclid Collaboration 2023, MNRAS, 520, 3529
Finkelstein, S. L., Dickinson, M., Ferguson, H. C., et al. 2017, The Cosmic Evolution Early Release Science (CEERS) Survey, JWST Proposal ID 1345. Cycle 0 Early Release Science #1345, STScI
Fontana, A., DOdorico, S., Poli, F., et al. 2000, AJ, 120, 2206
Förster Schreiber, N. M., & Wuyts, S. 2020, ARA&A, 58, 661
Franco, M., Elbaz, D., Bthermin, M., et al. 2018, A&A, 620, A152
Franco, M., Elbaz, D., Zhou, L., et al. 2020, A&A, 643, A30
Fritz, J., Franceschini, A., & Hatziminaoglou, E. 2006, MNRAS, 366, 767
Gardner, J. P., Mather, J. C., Clampin, M., et al. 2006, SSRv, 123, 485
Giacconi, R., Zirm, A., Wang, J., et al. 2002, ApJS, 139, 369
Giavalisco, M., Ferguson, H. C., Koekemoer, A. M., et al. 2004, ApJL, 600, L93

Gillman, S., Gullberg, B., Brammer, G., et al. 2023, A&A, 676, A26
Granato, G. L., Zotti, G. D., Silva, L., Bressan, A., & Danese, L. 2004, ApJ, 600, 580
Grazian, A., Fontana, A., Santis, C. D., et al. 2006, A&A, 449, 951
Grogin, N. A., Kocevski, D. D., Faber, S. M., et al. 2011, ApJS, 197, 35
Gullberg, B., Smail, I., Swinbank, A. M., et al. 2019, MNRAS, 490, 4956
Guo, Y., Ferguson, H. C., Giavalisco, M., et al. 2013, ApJS, 207, 24
Hainline, L. J., Blain, A. W., Smail, I., et al. 2011, ApJ, 740, 96
Harris, C. R., Millman, K. J., van der Walt, S. J., et al. 2020, Natur, 585, 357
Hatsukade, B., Kohno, K., Yamaguchi, Y., et al. 2018, PASJ, 70, 105
Hatton, S., Devriendt, J. E. G., Ninin, S., et al. 2003, MNRAS, 343, 75
Hughes, D. H., Serjeant, S., Dunlop, J., et al. 1998, Natur, 394, 241
Hunt, L. K., De Looze, I., Boquien, M., et al. 2019, A&A, 621, A51
Hunter, J. D. 2007, CSE, 9, 90
Hnig, S. F., Kishimoto, M., Tristram, K. R. W., et al. 2013, ApJ, 771, 87
Ivezic, Ž., Kahn, S. M., Tyson, J. A., et al. 2019, ApJ, 873, 111
Jakobsen, P., Ferruit, P., Alves de Oliveira, C., et al. 2022, A&A, 661, A80
Jones, E., Oliphant, T., Peterson, P., et al. 2001, SciPy: Open Source Scientific Tools for Python
Kartaltepe, J. S., Rose, C., Vanderhoof, B. N., et al. 2023, ApJL, 946, L15
Koekemoer, A. M., Faber, S. M., Ferguson, H. C., et al. 2011, ApJS, 197, 36
Laigle, C., McCracken, H. J., Ilbert, O., et al. 2016, ApJS, 224, 24
Lapi, A., Raimundo, S., Aversa, R., et al. 2014, ApJ, 782, 69
Laureijs, R., Amiaux, J., Arduini, S., et al. 2011, arXiv:1110.3193
Lawrence, A., Warren, S. J., Almaini, O., et al. 2007, MNRAS, 379, 1599
Leisawitz, D., Hyde, T. T., Rinehart, S. A., & Weiss, M. 2008, Proc. SPIE, 7010, 701028
Lelli, F., McGaugh, S. S., & Schombert, J. M. 2016, AJ, 152, 157
Liao, C.-L., Chen, C.-C., Wang, W.-H., et al. 2024, ApJ, 961, 226
Lilly, S. J., Eales, S. A., Gear, W. K. P., et al. 1999, ApJ, 518, 641
Ling, C.-T., Goto, T., Kim, S. J., et al. 2024, MNRAS, 528, 6025
Liu, D., Daddi, E., Dickinson, M., et al. 2018, ApJ, 853, 172
Long, A. S., Antwi-Danso, J., Lambrides, E. L., et al. 2024, ApJ, 970, 68
Lower, S., Narayanan, D., Leja, J., et al. 2020, ApJ, 904, 33
Lu, S., Zhu, K., Cappellari, M., et al. 2023, MNRAS, 526, 1022
Madau, P. 1995, ApJ, 441, 18
Mancuso, C., Lapi, A., Shi, J., et al. 2016, ApJ, 833, 152
Maraston, C. 2005, MNRAS, 362, 799
McElwain, M. W., Feinberg, L. D., Perrin, M. D., et al. 2023, PASP, 135, 058001
Merlin, E., Santini, P., Paris, D., et al. 2024, A&A, 691, A240
Michałowski, M. J., Dunlop, J. S., Cirasuolo, M., et al. 2012, A&A, 541, A85
Mitra, D., Negrello, M., DeZotti,, G., & Cai, Z.-Y. 2024, MNRAS, 530, 2292
Noll, S., Burgarella, D., Giovannoli, E., et al. 2009, A&A, 507, 1793
Pantoni, L., Lapi, A., Massardi, M., et al. 2021, MNRAS, 504, 928
Pearson, E. A., Eales, S., Dunne, L., et al. 2013, MNRAS, 435, 2753
Pforr, J., Maraston, C., & Tonini, C. 2012, MNRAS, 422, 3285
Pforr, J., Maraston, C., & Tonini, C. 2013, MNRAS, 435, 1389
Planck Collaboration VI 2020, A&A, 641, A6
Rieke, M. J., Kelly, D. M., Misselt, K., et al. 2023, PASP, 135, 028001
Rigby, J., Perrin, M., McElwain, M., et al. 2023, PASP, 135, 048001
Rowlands, K., Dunne, L., Dye, S., et al. 2014, MNRAS, 441, 1017
Scoville, N., Aussel, H., Brusa, M., et al. 2007, ApJS, 172, 1
Simpson, J. M., Smail, I., Swinbank, A. M., et al. 2017, ApJ, 839, 58
Simpson, J. M., Swinbank, A. M., Smail, I., et al. 2014, ApJ, 788, 125
Siringo, G., Kreysa, E., Kovcs, A., et al. 2009, A&A, 497, 945
Smail, I., Ivison, R. J., & Blain, A. W. 1997, ApJL, 490, L5
Straatman, C. M. S., Spitler, L. R., Quadri, R. F., et al. 2016, ApJ, 830, 51
Swinbank, A. M., Chapman, S. C., Smail, I., et al. 2006, MNRAS, 371, 465
Swinbank, A. M., Harrison, C. M., Trayford, J., et al. 2017, MNRAS, 467, 3140
Swinbank, A. M., Simpson, J. M., Smail, I., et al. 2014, MNRAS, 438, 1267
Tan, Q.-H., Daddi, E., Magnelli, B., et al. 2024, Natur, 636, 69
Thomas, D., Maraston, C., Schawinski, K., Sarzi, M., & Silk, J. 2010, MNRAS, 404, 1775
Toft, S., Smolčić, V., Magnelli, B., et al. 2014, ApJ, 782, 68
Turner, O. J., Cirasuolo, M., Harrison, C. M., et al. 2017, MNRAS, 471, 1280
van der Walt, S., Colbert, S. C., & Varoquaux, G. 2011, CSE, 13, 22
Waskom, M. 2021, JOSS, 6, 3021
Wiklind, T., Conselice, C. J., Dahlen, T., et al. 2014, ApJ, 785, 111
Williams, C. C., Curtis-Lake, E., Hainline, K. N., et al. 2018, ApJS, 236, 33
Wisnioski, E., Förster Schreiber, N. M., Fossati, M., et al. 2019, ApJ, 886, 124
Yamaguchi, Y., Kohno, K., Hatsukade, B., et al. 2020, PASJ, 72, 69
Yang, Q., Shen, Y., Liu, X., et al. 2020, ApJ, 900, 58